The birth of a relativistic jet following the disruption of a star by a cosmological black hole

Pasham, D.R.; Lucchini, M.; Laskar, T.; Gompertz, B.P.; Srivastav, S.; Nicholl, M.; ... ; Yang, S.

Citation

Pasham, D. R., Lucchini, M., Laskar, T., Gompertz, B. P., Srivastav, S., Nicholl, M., … Yang, S. (2023). The birth of a relativistic jet following the disruption of a star by a cosmological black hole. *Nature Astronomy*, 7, 88-104. doi:10.1038/s41550-022-01820-x nature astronomy

Article

https://doi.org/10.1038/s41550-022-01820-x

The Birth of a Relativistic Jet Following the Disruption of a Star by a Cosmological Black Hole

Received: 27 May 2022

Accepted: 30 September 2022

A list of authors and their affiliations appears at the end of the paper

A black hole can launch a powerful relativistic jet after it tidally disrupts a star. If this jet fortuitously aligns with our line of sight, the overall brightness is Doppler boosted by several orders of magnitude. Consequently, such on-axis relativistic tidal disruption events have the potential to unveil cosmological (redshift $z > 1$) quiescent black holes and are ideal test beds for understanding the radiative mechanisms operating in super-Eddington jets. Here we present multiwavelength (X-ray, UV, optical and radio) observations of the optically discovered transient AT 2022cmc at $z = 1.193$. Its unusual X-ray properties, including a peak observed luminosity of $\gtrsim 10^{48}$ erg s^{-1}, systematic variability on timescales as short as 1,000 s and overall duration lasting more than 30 days in the rest frame, are traits associated with relativistic tidal disruption events. The X-ray to radio spectral energy distributions spanning 5–50 days after discovery can be explained as synchrotron emission from a relativistic jet (radio), synchrotron self-Compton (X-rays) and thermal emission similar to that seen in low-redshift tidal disruption events (UV/optical). Our modelling implies a beamed, highly relativistic jet akin to blazars but requires extreme matter domination (that is, a high ratio of electron-to-magnetic-field energy densities in the jet) and challenges our theoretical understanding of jets.

AT 2022cmc was discovered in the optical waveband by the Zwicky Transient Facility (ZTF)[1] on 11 February 2022 as a fast-evolving transient, and was publicly reported to the Gamma-ray Coordinates Network on 14 February 2022[2]. We confirmed the rapid evolution of this transient in the Asteroid Terrestrial-impact Last Alert System (ATLAS) survey data with a non-detection 24 h before the ZTF discovery and a subsequent decline of 0.6 mag d^{-1} (ref. [3]). A radio counterpart was identified in Karl G. Jansky Very Large Array (VLA) observations on 15 February 2022[4]. Although the optical spectrum taken on 16 February 2022 revealed a featureless continuum[5], spectral features were detected in subsequent spectra taken 1 d later with the European Southern Observatory's (ESO) Very Large Telescope (VLT)[6] and Keck/DEIMOS[7]. In particular, the detection of [O III] λ5007 emission and Ca II, Mg II and Fe II absorption lines yielded a redshift measurement of $z = 1.193$, or a luminosity distance of 8.45 Gpc (refs. [6,7]). The source did not have a neutrino counterpart[8]. Our follow-up X-ray (0.3–5 keV) observations with the Neutron star Interior Composition ExploreR (NICER) on 16 February 2022 revealed a luminous X-ray counterpart[9]. We also triggered additional multiwavelength observations with numerous facilities, including AstroSat, NICER and The Neil Gehrels Swift Observatory (Swift) in the X-ray and the UV wavebands (Extended Data Figs. 1–3). We obtained an optical spectrum with ESO/VLT (Extended Data Fig. 4) and imaging with several optical telescopes (for example, see Extended Data Fig. 5 and Supplementary Data 1). In the radio band, we acquired multifrequency data with the VLA, the Arcminute Microkelvin Imager-Large Array (AMI-LA) and the European Very Long Baseline Interferometry Network (EVN; see 'Observations and data analysis' in the Methods for details of these observations). We adopted modified Julian date (MJD) 59621.4458 (the

e-mail: drreddy@mit.edu

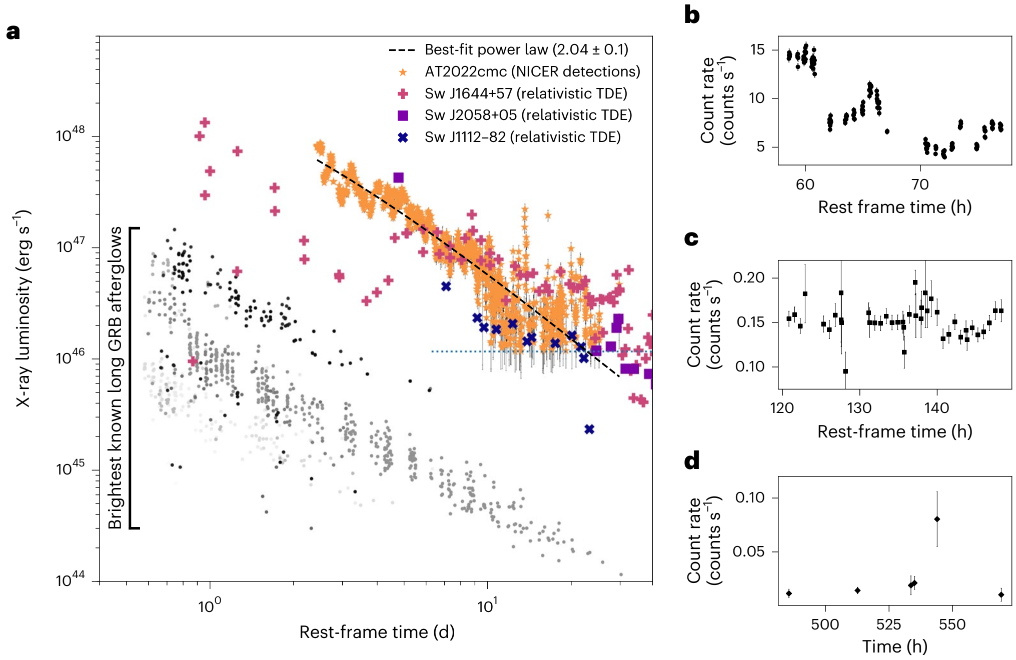

Fig. 1 | AT 2022cmc's X-ray evolution on various timescales at different epochs. a, AT 2022cmc's k-corrected unabsorbed 0.3–10 keV X-ray luminosity in comparison with the most luminous known X-ray transients. The grey-scale circles are a sample of 56 of the most luminous gamma-ray burst (GRB) X-ray afterglows known[62]. Only data past 50,000 rest-frame s are shown to highlight the late-time emission from these afterglows. AT 2022cmc is substantially more luminous than any known GRB afterglow and its X-ray luminosity is only comparable to previously known relativistic jetted TDEs Sw J1644+57, Sw J2058+05 and Sw J1112–82. The dotted horizontal blue line at 1.2×10^{46} erg s^{-1} is an estimate of NICER's background-limited sensitivity limit for sources at $z = 1.193$. See 'GRB and TDE comparison data' in the Methods for a description of the comparison sample used in this figure. **b**, AT 2022cmc's sample NICER (0.3–5 keV) light curve highlighting variability on hour timescales (see also Extended Data Fig. 6). **c**, AT 2022cmc's AstroSat (0.5–7 keV) light curve showing variability on hour timescales. **d**, AT 2022cmc's Swift X-ray (0.3–8 keV) light curve highlighting a flare more than 3 weeks (in the rest frame) after the initial discovery. All the light curves are background-corrected. In **b**–**d**, background-corrected count rates versus rest-frame time since MJD 59621.4458 are shown. All error bars represent 1σ uncertainties. These data are provided as supplementary files ("Fig1data.tar").

discovery epoch) as the reference time throughout the Article and all relative times are in the observer frame unless otherwise mentioned.

The most striking property of AT 2022cmc is its high isotropic peak X-ray luminosity of $\gtrsim 10^{48}$ erg s^{-1} (orange data points in Fig. 1a). High apparent luminosity can be caused by gravitational lensing; however, this contributes no more than a 10% enhancement for AT 2022cmc (see 'Gravitational lens magnification by a foreground structure' in the Methods). AT 2022cmc's second compelling aspect is its rapid X-ray variability over a wide range of timescales: during the weeks after the initial optical discovery, it showed variability on timescales ranging from 1,000 s to many days (Fig. 1a–d and Extended Data Fig. 6; see also 'Shortest X-ray variability timescale' in the Methods). The X-ray spectrum is generally consistent with a simple power-law model with the best-fit photon index varying between 1.3 and 1.9 (Extended Data Fig. 3 and Table 1). There are intermittent rapid flares during which the X-ray spectrum deviates from a power-law model (see 'γ-rays and X-rays/NICER' in the Methods). AT 2022cmc's observed optical and UV light curves exhibit three phases after reaching their peaks: an early slow decline phase at $\lesssim 3.1$ d with a decline rate $\alpha \approx -0.5$ steepening further to $\alpha \approx -2.5$ at ~6.4 d, followed by a shallow decline ($\alpha \approx -0.3$) at $\gtrsim 6.4$ d (Fig. 2). We use the convention $F_\nu(\nu) \propto t^\alpha \nu^\beta$ throughout, where F_ν is the flux per unit frequency, ν is the observed frequency, α is the temporal decay rate, t is the time since peak, and β is the spectral index. An optical spectrum taken at ~15 d shows a featureless blue continuum, which could be fitted using a thermal model with a rest-frame temperature of ~3×10^4 K (Extended Data Fig. 4). The 15 GHz flux density, on the other hand, was rising monotonically with time at $\gtrsim 10$ d (see Fig. 2). The radio spectrum seems to be consistent with the standard synchrotron self-absorption process from a single-emitting region (for example, see ref. [10]).

AT 2022cmc's high apparent X-ray energy output, extreme luminosity variations (a factor of ~500 over a few weeks; see the grey and black data points in Fig. 2) and fast variability require an active central engine. Such an engine can be naturally explained by an extreme accretion episode onto a black hole, which could be due to a stellar tidal disruption[11]. Among transients, AT 2022cmc's apparent X-ray luminosity and evolution are only comparable to Sw J1644+57 (for example, ref. [12]), Sw J2058.4+0516 (for example, refs. [13,14]) and Sw J1112.2-8238 (ref. [15]), the three tidal disruption events (TDEs) with relativistic jets. AT 2022cmc's thermal optical emission with temperature of ~2.3×10^4 K is often seen in low-redshift ($z \lesssim 0.2$) TDEs[16] and could be from a newly formed accretion disk (for example, ref. [17]), reprocessing (for example, ref. [18]) or from debris stream self-collisions (for example, refs. [19,20]). The high optical/UV luminosity of ~2×10^{45} erg s^{-1} at d 15–16 post-discovery (Fig. 3) is only comparable to the extreme TDE candidate ASASSN-15lh (ref. [21]). From the rich literature on accretion-driven outbursts from stellar-mass black holes in X-ray binaries, we now know that accretion and consequently related ejection can lead to variability on a wide range of timescales (see ref. [22] and references therein). Thus, accretion/ejection following a tidal disruption could also naturally explain AT 2022cmc's observed flux variability over a wide range of timescales.

Given the similar X-ray luminosity and variability to Sw J1644+57, the best-studied TDE with a relativistic jet, we modelled AT 2022cmc's data under the jet paradigm. In a standard jet scenario, the radio through infrared/optical/UV data are dominated by non-thermal synchrotron emission[23,24]. However, extrapolating AT 2022cmc's radio/optical/UV data to higher frequencies does not provide emission consistent with the observed X-ray flux (see 'Preliminary considerations' in the Methods and Extended Data Fig. 7), suggesting that the

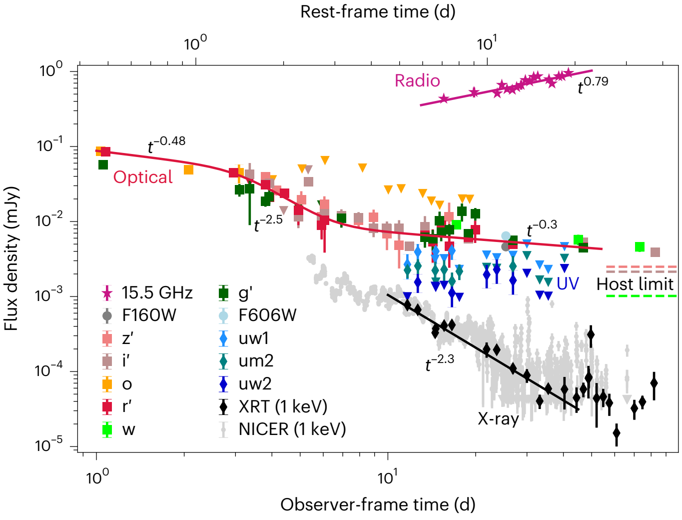

Fig. 2 | Multiwavelength light curves of AT 2022cmc. NICER, Swift/XRT and UVOT (diamonds), Hubble Space Telescope (HST; circles), ground-based optical (squares) and radio (stars) light curves of AT 2022cmc span ~1–83 d after discovery. Also shown are the single/smoothly broken power-law model fits to the Swift/XRT (black), r′-band (red) and 15 GHz (violet) light curves. Their corresponding best-fit indices are also indicated. The Swift and NICER X-ray light curves have been converted from 0.3–5 keV observer-frame observed flux to flux density at 1 keV using the average and time-resolved X-ray spectral fits, respectively (see 'Swift/XRT' and 'NICER' in the Methods). The optical light curve exhibits a steep decay at ~1–3 d in the rest frame, followed by a plateau, during which the radio light curve is seen to rise. Dashed lines indicate w-, i- and z-band upper limits on underlying host emission obtained from deep stacks of Pan-STARRS pre-discovery images (see 'Constraints on host luminosity' in the Methods and Extended Data Fig. 5). Upper limits are indicated by inverted triangles. All the photometry presented in this figure represents observed values that were corrected for Galactic extinction. These data are provided as a supplementary file. The multifrequency VLA SED taken on 27 February 2022 is shown in Fig. 3. All error bars represent 1σ uncertainties. uw1, uw2, and um2 are the UV filters on Swift/UVOT.

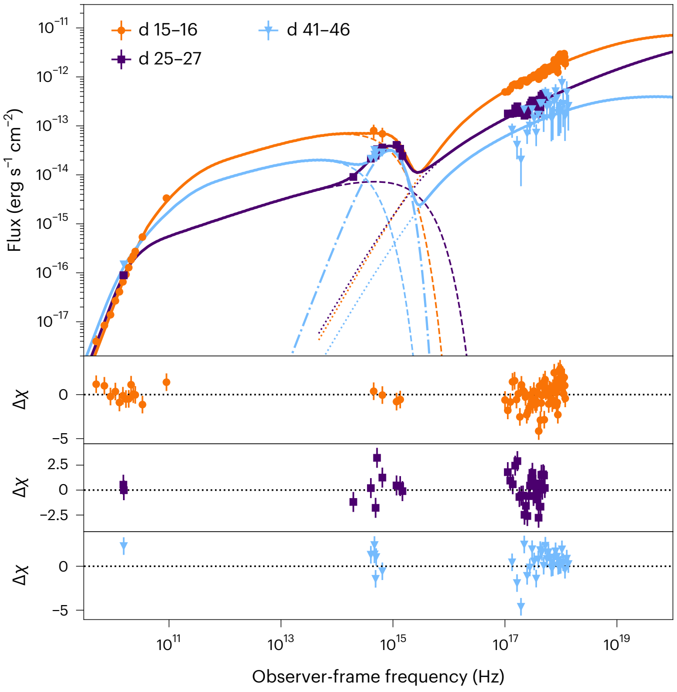

Fig. 3 | AT 2022cmc's multiwavelength SEDs and their best-fit models. SEDs from three epochs were fitted with a single-zone jet model comprising synchrotron (dashed), SSC (dotted) and blackbody (dash-dot) emission components. The radio data are consistent with optically thick synchrotron emission, while the X-ray emission is well fitted by SSC originating from the same emitting region. The strength of the SSC component implies a strongly matter-dominated jet, with $U_e/U_B \geq 10^2$, where U_e is the energy density of the electrons and U_B the energy density of the magnetic field B. The optical data at 25–27 and 41–46 d after discovery exhibit an excess over the synchrotron + SSC model; as a result, we added a blackbody component of temperature $T_{\rm bb} = 2.3 \times 10^4$ K (measured in the source frame) and luminosity $L_{\rm bb} = 1.7 \times 10^{45}$ erg s^{-1}. The corresponding radius is $R_{\rm bb} = 2.8 \times 10^{15}$ cm. Owing to a lack of optical/UV constraints on d 15–16, this component was assumed to remain constant between days 15 and 46 (see 'Multiwavelength SED modelling' in the Methods and Table 2). The data in this figure are available as a supplementary file. All error bars represent 1σ uncertainties.

high-energy emission originates from a second component. Similar to blazars, this second component could naturally arise from inverse Compton scattering of either local synchrotron photons (synchrotron self-Compton (SSC)) or photons originating outside the jet (external Compton). In both cases, the photons would interact with the electrons in the jet. We therefore investigated these scenarios by fitting three observed time-averaged spectral energy distributions (SEDs) with good multiwavelength coverage (d 15–16, 25–27 and 41–46) with a simple jet model consisting of a spherical, homogeneous emitting region, similar to the approach commonly used to infer the properties of the emitting region in blazars[25–27]. The rapid X-ray variability on timescales of tens of minutes and self-absorbed radio spectrum indicate that the observed radio and X-ray emission originate from a compact region, rather than in an extended outflow, further motivating our choice of a single-zone approximation.

We tested two emission models, one in which the only radiative mechanisms considered were synchrotron and SSC (model 1), and one that included external Compton of thermal photons originating outside the jet (model 2). Model 1 (the synchrotron + SSC model), shown in Fig. 3, provided an acceptable fit to the radio through X-ray SEDs (χ^2/d.f. = 2.2), albeit with extreme parameters (see below). Model 2, on the other hand, was disfavoured because it could not explain the radio flux while still resulting in similarly extreme parameters (see 'Modelling results' in the Methods and Extended Data Fig. 8). The best-fitting parameters for both models are reported in Table 2. Contour plots between the parameters of model 1 are shown in Extended Data Fig. 9. We caution that these numbers could change substantially with a more complex and physical model, and the fits presented here purely constitute a check that the data are consistent with the emission from a relativistic jet.

The main trend emerging from model 1 is that the jet has to be very powerful (~$10^{46–47}$ erg s^{-1}, depending on its composition) and strongly beamed: the Doppler factor is $\delta = [\Gamma_{\rm j}\,(1-\beta_{\rm j}\,\cos(\theta)]^{-1} \approx 100$, where $\Gamma_{\rm j} \approx 86$ is the jet bulk Lorentz factor, $\beta_{\rm j}$ the corresponding speed in units of the speed of light and θ is the jet viewing angle. On the other hand, model 2 requires a lower jet power (~10^{45} erg s^{-1}) and a smaller $\Gamma_{\rm j} \approx 5$ and $\delta \approx 10$. Under the jet paradigm, the observed X-rays and their variability arise from within the jet; as a result, a size constraint can be compared to the observed variability timescale to check for consistency. On the basis of a simple causality argument, we require the size of the emitting region to be smaller than the minimum variability timescale × speed of light × Doppler factor ≈ 1,000 s × 3 × 10^{10} × δ cm ≈ 3 × 10^{13} × δ cm for our case, where δ accounts for relativistic beaming[28]. The emitting region inferred had an estimated radius of ~$10^{15–16}$ cm from model 1 and ~10^{14} cm from model 2. Both of these estimates were consistent with the hour-long variability timescale observed by NICER but are only marginally consistent with ~1,000 s X-ray variations. Such rapid variability has also been observed in some extreme blazar flares (for example, refs. [29,30]), and is inconsistent with the simple homogeneous, time-independent single-zone model presented here. Instead, it can

https://doi.org/10.1038/s41550-022-01820-x

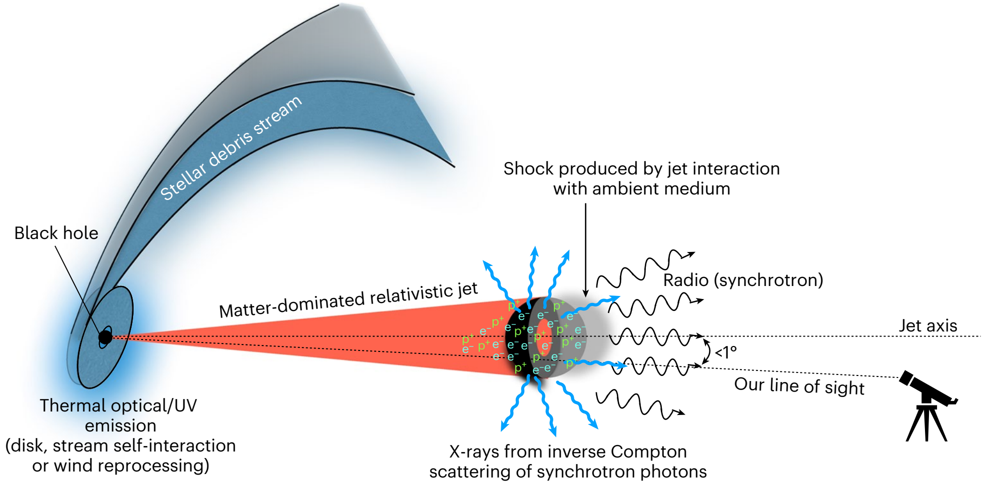

Fig. 4 | Schematic of our proposed scenario for AT 2022cmc. A mass-loaded, highly relativistic jet with $\Gamma_j \approx 80$ can explain AT 2022cmc's multiwavelength SED with radio emission originating from synchrotron processes and X-rays from SSC (see 'Multiwavelength SED modelling' in the Methods and Table 2). The optical/UV emission part of the SED on d 25 is consistent with thermal emission with a temperature of ~2.3×10^4 K and a luminosity of 2×10^{45} erg s^{-1} (in the rest frame). These are comparable to low-z non-jetted TDEs[50]. It could originate from an accretion disk, reprocessing by an outflow (for example ref. [18]) or from stellar debris stream self-collisions[20]. Our viewing angle with respect to the jet axis was estimated from our SED modelling to be <1° (Table 2).

be reproduced using a complex inhomogeneous, time-dependent model[31]. However, applying such a model to AT 2022cmc is beyond the scope of this work.

Both models 1 and 2 require a strong SSC contribution to match the X-ray flux. For this to happen, we require a strongly matter-dominated jet; that is, most of the power is carried by the electrons and protons within the jet, rather than by the magnetic field. Such a matter-dominated flow is in tension with the common theoretical paradigm that jets are magnetically dominated at their launching point, and then accelerate by turning the magnetic field into bulk kinetic energy until they reach rough equipartition[32,33], but is in line with ref. [34], which proposed a structured, radiation-driven jet powered by super-Eddington accretion. The jet collimation could be provided by the pressure of the surrounding accretion flow, which is highly inflated during the super-Eddington phase (for example, refs. [34–37]). These issues are also often encountered when modelling blazar jets with a dominant SSC component[27,38], as well as M87[39], suggesting the need for more complex models. A schematic of our proposed, albeit simple, model (synchrotron + SSC + thermal optical/UV) is shown in Fig. 4.

Finally, our SED modelling implies that the underlying physics in AT 2022cmc's jet may be distinct from that of Sw J1644+57 and Sw J2058+05, as in those sources SSC cannot produce the observed X-ray emission[40]. It has been argued that in Sw J1644+57 the X-rays originate from a corona/base of a jet through external inverse Compton scattering by a photon field coming from either the disk (for example, refs. [12,41]) or from the disk wind (for example, ref. [40]). This external inverse Compton model has also been successfully applied to Sw J2058+05[41,42]. Instead, in AT 2022cmc external Compton cannot explain the observed X-rays (see 'Modelling results' in the Methods), and thus its high-energy emission seems to be driven by different mechanisms than previous relativistic TDEs.

Although our models provide strong evidence that the multiwavelength emission of AT 2022cmc is powered by a relativistic jet, they also show that a more complex model is required to probe the physics of the jet self-consistently. The data presented in this article provide an opportunity to explore detailed jet physics at extreme mass accretion rates.

As a relativistic jet can explain the multiwavelength properties of AT 2022cmc, we next investigated the plausible mass of the black hole engine. At the low-mass end, ~10 $M_\odot$, the most powerful known jets are launched following GRBs. A GRB afterglow interpretation can be ruled out due to the: (1) unusually high X-ray luminosity; (2) fast variability out to weeks after discovery; (3) overall duration of AT 2022cmc; and (4) non-synchrotron SED (see 'Arguments against a GRB afterglow' in the Methods for a more thorough/detailed discussion). We disfavour a blazar flare/outburst for three reasons. First, the light curves of blazar flares show stochastic variability on top of a fairly constant low flux (for example, ref. [31]), whereas AT 2022cmc shows a smooth decay structure typical of transients powered by a sudden (and possibly subsequently sustained) deposition of energy. Second, all blazar classes have a flat radio spectrum, $F(\nu) \propto \nu^0$, whereas AT 2022cmc exhibits a strongly self-absorbed spectrum with $F(\nu) \propto \nu^2$. Finally, a large-amplitude optical brightness enhancement of ~4 magnitudes (see 'Constraints on host luminosity' in the Methods) is unusual for blazars (for example, compare with ref. [31]). In addition, there is no gamma-ray source detected by Fermi/Large Area Telescope (LAT) within 1° diameter of AT 2022cmc.

A TDE is largely characterized by the pericentre distance (the closest approach between the star and the black hole), the stellar properties and the black hole mass. The pericentre distance does not affect the accretion rate if the disruption is full (for example, refs. [43–46]), whereas if it is partial there is a steep fall in luminosity with increasing distance (for example, refs. [44,47,48]). For a star of radius $R_\star$ and mass $M_\star$ and a black hole of mass M, the characteristic TDE accretion rate is $\propto (M_\star/R_\star)^{3/2}(M/M_\star)^{-1/2}$. For a main sequence star with $R_\star \propto M_\star$ the luminosity is therefore $\propto M_\star^{1/2}$, and a very massive (and rare) star is needed to substantially modify the accretion rate (for example, see fig. 4 of ref. [49]). On the other hand, the Eddington ratio for a TDE scales as $M^{-3/2}$, and a modest decrease in black hole mass yields a large increase in the Eddington fraction. Given these considerations, and the approximate scaling of the X-ray luminosity as $\propto t^{-9/4}$ (ref. [47]), we suggest that AT 2022cmc could have been powered by the partial disruption (near the full disruption threshold) of a dwarf star by a relatively low-mass black hole and its super-Eddington accretion.

Although non-relativistic TDEs are now routinely discovered (roughly one every few weeks) in the nearby Universe ($z \lesssim 0.2$)[16,50], Doppler-boosted TDEs such as AT 2022cmc can push the redshift

Table 1 | Summary of the best-fit parameters from time-resolved X-ray energy spectral modelling of AT 2022cmc

Start (MJD)	End (MJD)	Exposure (ks)	FPMs	Phase	Index	log[Integ. lum. (erg s^{-1})]	log[Obs. lum. (erg s^{-1})]	Count rate (counts s−1)	χ^2/number of bins
59626.75	59627.25	6.36	52	E0	$1.5^{+0.01}_{-0.01}$	$47.825^{+0.003}_{-0.003}$	$47.247^{+0.003}_{-0.002}$	0.2354±0.0011	68.3/77
59627.25	59627.75	5.28	52	E1	$1.58^{+0.01}_{-0.01}$	$47.715^{+0.004}_{-0.004}$	$47.099^{+0.002}_{-0.004}$	0.1733±0.0011	97.4/73
59627.75	59628.25	4.8	52	E2	$1.66^{+0.01}_{-0.01}$	$47.484^{+0.005}_{-0.005}$	$46.832^{+0.002}_{-0.004}$	0.0971±0.001	112.6/72
59628.25	59628.75	5.76	52	E3	$1.65^{+0.01}_{-0.01}$	$47.613^{+0.004}_{-0.004}$	$46.965^{+0.004}_{-0.002}$	0.1309±0.001	70.0/73
59628.75	59629.25	3.48	52	E4	$1.64^{+0.01}_{-0.01}$	$47.496^{+0.006}_{-0.006}$	$46.851^{+0.004}_{-0.004}$	0.1008±0.0013	83.7/71
59629.25	59629.75	2.28	52	E5	$1.63^{+0.02}_{-0.02}$	$47.39^{+0.008}_{-0.008}$	$46.751^{+0.006}_{-0.005}$	0.0801±0.0019	58.3/66
59629.75	59630.25	2.64	52	E6	$1.69^{+0.02}_{-0.02}$	$47.405^{+0.008}_{-0.008}$	$46.737^{+0.006}_{-0.004}$	0.0792±0.0018	70.4/67
59630.25	59630.75	2.76	51	E7	$1.69^{+0.02}_{-0.02}$	$47.483^{+0.007}_{-0.007}$	$46.818^{+0.005}_{-0.004}$	0.0954±0.0017	64.2/69
59630.75	59631.25	3.84	52	E8	$1.64^{+0.01}_{-0.01}$	$47.427^{+0.006}_{-0.006}$	$46.786^{+0.004}_{-0.006}$	0.0865±0.0014	63.0/71
59631.25	59631.75	5.64	52	E9	$1.61^{+0.01}_{-0.01}$	$47.377^{+0.005}_{-0.005}$	$46.747^{+0.004}_{-0.003}$	0.0785±0.0009	86.8/72
59631.75	59632.25	2.76	52	E10	$1.65^{+0.02}_{-0.02}$	$47.397^{+0.007}_{-0.007}$	$46.748^{+0.004}_{-0.004}$	0.0801±0.0017	69.5/68
59632.25	59632.75	3.72	52	E11	$1.54^{+0.02}_{-0.02}$	$47.436^{+0.007}_{-0.007}$	$46.836^{+0.005}_{-0.006}$	0.0696±0.0012	73.1/71
59632.75	59633.25	3.36	52	E12	$1.56^{+0.02}_{-0.02}$	$47.261^{+0.007}_{-0.007}$	$46.654^{+0.005}_{-0.006}$	0.0621±0.0014	66.2/68
59633.25	59633.75	3.12	52	E13	$1.52^{+0.02}_{-0.02}$	$47.247^{+0.007}_{-0.007}$	$46.658^{+0.005}_{-0.005}$	0.0617±0.0014	74.5/68
59633.75	59634.25	6.36	52	E14	$1.48^{+0.01}_{-0.01}$	$47.253^{+0.005}_{-0.005}$	$46.684^{+0.003}_{-0.003}$	0.0643±0.0008	71.4/72
59634.25	59634.75	4.44	52	E15	$1.52^{+0.02}_{-0.02}$	$47.136^{+0.007}_{-0.007}$	$46.55^{+0.007}_{-0.006}$	0.048±0.001	79.7/69
59634.75	59635.25	2.28	52	E16	$1.54^{+0.02}_{-0.02}$	$47.21^{+0.009}_{-0.009}$	$46.614^{+0.006}_{-0.007}$	0.056±0.0019	62.5/63
59635.25	59635.75	1.8	52	E17	$1.55^{+0.03}_{-0.03}$	$47.128^{+0.01}_{-0.011}$	$46.529^{+0.008}_{-0.008}$	0.0463±0.0024	50.6/58
59635.75	59636.25	2.16	52	E18	$1.54^{+0.03}_{-0.03}$	$47.009^{+0.011}_{-0.011}$	$46.414^{+0.008}_{-0.011}$	0.0355±0.002	45.3/58
59636.25	59636.75	1.2	52	E19	$1.87^{+0.05}_{-0.05}$	$46.992^{+0.02}_{-0.02}$	$46.24^{+0.013}_{-0.013}$	0.0272±0.0033	32.4/40
59636.75	59637.25	2.52	52	E20	$1.73^{+0.03}_{-0.03}$	$47.001^{+0.013}_{-0.013}$	$46.315^{+0.01}_{-0.007}$	0.0306±0.0016	50.2/54
59637.25	59637.75	2.28	52	E21	$1.31^{+0.03}_{-0.03}$	$46.934^{+0.011}_{-0.011}$	$46.436^{+0.013}_{-0.01}$	0.0349±0.0018	125.5/62
59637.75	59638.25	0.84	52	E22	$1.53^{+0.06}_{-0.05}$	$46.912^{+0.02}_{-0.02}$	$46.319^{+0.016}_{-0.015}$	0.0288±0.0053	34.9/39
59638.25	59638.75	1.44	49	E23	$1.59^{+0.04}_{-0.04}$	$46.982^{+0.015}_{-0.015}$	$46.361^{+0.013}_{-0.008}$	0.0322±0.0029	33.5/47
59638.75	59639.25	2.88	52	E24	$1.61^{+0.03}_{-0.03}$	$46.946^{+0.011}_{-0.011}$	$46.317^{+0.01}_{-0.006}$	0.0293±0.0015	64.2/60
59639.25	59639.75	2.4	49	E25	$1.53^{+0.04}_{-0.04}$	$46.886^{+0.013}_{-0.013}$	$46.295^{+0.007}_{-0.01}$	0.0272±0.0017	58.0/56
59639.75	59640.25	3.12	52	E26	$1.57^{+0.03}_{-0.03}$	$46.921^{+0.011}_{-0.011}$	$46.31^{+0.009}_{-0.006}$	0.0284±0.0013	66.2/59
59640.25	59640.75	2.76	52	E27	$1.53^{+0.03}_{-0.03}$	$46.999^{+0.01}_{-0.01}$	$46.405^{+0.008}_{-0.01}$	0.0347±0.0015	48.6/59
59640.75	59641.25	2.64	49	E28	$1.57^{+0.03}_{-0.03}$	$46.927^{+0.012}_{-0.012}$	$46.316^{+0.013}_{-0.009}$	0.0286±0.0014	42.5/56
59641.25	59641.75	3.0	52	E29	$1.54^{+0.03}_{-0.03}$	$46.861^{+0.012}_{-0.012}$	$46.263^{+0.009}_{-0.012}$	0.0252±0.0012	63.7/56
59641.75	59642.25	4.44	52	E30	$1.52^{+0.03}_{-0.03}$	$46.765^{+0.011}_{-0.011}$	$46.177^{+0.01}_{-0.007}$	0.0206±0.0009	66.0/61
59642.25	59642.75	0.24	52	E31	$1.51^{+0.15}_{-0.16}$	$46.747^{+0.052}_{-0.053}$	$46.166^{+0.042}_{-0.035}$	0.0208±0.0175	11.8/12
59642.75	59643.25	2.4	48	E32	$1.47^{+0.05}_{-0.05}$	$46.752^{+0.016}_{-0.016}$	$46.187^{+0.014}_{-0.011}$	0.021±0.0019	70.5/56

0.3–5.0 keV NICER spectra were fitted with the tbabs*ztbabs*zashift(clumin*pow) model using XSPEC[55]. Start and End represent the start and end times (in MJD) of the interval used to extract a combined NICER spectrum. Exposure is the accumulated exposure time during this time interval. FPMs is the total number of active detectors minus the 'hot' detectors. Phase is the name used to identify the epoch. Index is the photon index of the power-law component. Integ. lum. is the integrated absorption-corrected power-law luminosity over 0.3–10 keV. Obs. lum. is the observed 0.3–5.0 keV luminosity. The count rate is the background-subtracted NICER count rate over 0.3–5.0 keV per FPM. All errors represent 1σ uncertainties. χ2/number of bins represents the best-fit χ2 and the number of spectral bins. The total χ2/d.f is 2,135.3/1956. A machine-readable version of this table is available as Supplementary Data 3.

barrier as they are orders of magnitude more luminous. AT 2022cmc's multiwavelength properties are consistent with a TDE with a relativistic jet closely aligned with our line of sight. All these factors bolster the exciting prospect of unveiling $z > 1$ TDEs, and consequently black holes, in the upcoming era of the LSST/Rubin observatory[51].

Methods

Observations and data analysis

The data presented in this work were acquired by different telescopes/instruments across the electromagnetic spectrum. Below we describe the data and the relevant reduction and analysis procedures.

Table 2 | Summary of the best-fitting jet models

Model	Date range (MJD)			Tied parameters
	59636.446–59638.446	**59636.446–59638.446**	**59662.446–59667.446**	
Model 1				
B (G)	$0.13^{+0.03}_{-0.03}$	$1.0^{+0.2}_{*} \times 10^{-2}$	$9.7^{+5.4}_{-3.5} \times 10^{-2}$	
R (cm)	$5.9^{+0.2}_{-0.1} \times 10^{15}$	$6.9^{+0.3}_{-0.3} \times 10^{15}$	$1.0^{*}_{-0.3} \times 10^{16}$	
n_e (cm^{-3})	973^{+195}_{-160}	2200^{+237}_{-205}	144^{+58}_{-38}	
γ_{max}	$5.0^{+1.2}_{-0.9} \times 10^{3}$	$3.2^{+1.8}_{-0.4} \times 10^{4}$	$3.4^{+1.4}_{-0.9} \times 10^{3}$	
γ_{min}				91^{+4}_{-4}
p				$2.21^{+0.05}_{-0.05}$
Γ_j				86^{+9}_{-10}
θ (°)				$0.5^{+0.1}_{*}$
L_{bb} (erg s^{-1})				$1.71^{+0.13}_{-0.11} \times 10^{45}$
T_{bb} (K)				$2.34^{+0.16}_{-0.14} \times 10^{4}$
δ				103
P_e (erg s^{-1})	5.3×10^{45}	2.0×10^{46}	2.0×10^{45}	
P_B (erg s^{-1})	1.6×10^{43}	1.5×10^{41}	2.6×10^{43}	
P_p (erg s^{-1})	3.6×10^{46}	1.1×10^{47}	1.5×10^{46}	
P_j (erg s^{-1})	4.1×10^{46}	1.3×10^{47}	1.7×10^{46}	
U_e/U_B	325	1.3×10^{5}	77	
R_{bb} (cm)				2.8×10^{15}
	59636.446–59638.446	**59636.446–59638.446**	**59662.446–59667.446**	**Tied parameters**
Model 2				
B (G)	$10.2^{+2.0}_{-1.6}$	18^{+5}_{-3}	36^{+14}_{-9}	
R (cm)	$1.16^{+0.12}_{-0.10} \times 10^{14}$	$6.0^{+0.9}_{-0.8} \times 10^{13}$	$2.2^{+0.4}_{-0.6} \times 10^{14}$	
n_e (cm^{-3})	$8.7^{+1.5}_{-1.3} \times 10^{7}$	$1.3^{+0.3}_{-0.3} \times 10^{8}$	$4.2^{+2.0}_{-1.5} \times 10^{6}$	
γ_{max}	$1.2^{+0.9}_{-0.4} \times 10^{4}$	$3.4^{+2.2}_{-1.3} \times 10^{3}$	$6.7^{+2.3}_{-1.7} \times 10^{2}$	
γ_{min}				$4.7^{+0.5}_{-0.4}$
p				$2.13^{+0.09}_{-0.08}$
Γ_j				5^{+1}_{-*}
θ (°)				$1.3^{+0.8}_{-0.6}$
L_{bb} (erg s^{-1})				$1.36^{+0.10}_{-0.08} \times 10^{45}$
T_{bb} (K)				$2.10^{+0.11}_{-0.10} \times 10^{4}$
δ				10.7
P_e (erg s^{-1})	4.5×10^{43}	2.3×10^{43}	7.6×10^{42}	
P_B (erg s^{-1})	1.6×10^{41}	1.4×10^{41}	6.9×10^{42}	
P_p (erg s^{-1})	5.0×10^{45}	2.0×10^{45}	8.2×10^{44}	
P_j (erg s^{-1})	5.1×10^{45}	2.0×10^{45}	8.4×10^{44}	
U_e/U_B	412	164	1.1	
R_{bb} (cm)				3.1×10^{15}

The emitting region magnetic field B, radius R, number density n_e and the maximum Lorentz factor of the particles γ_{max} were left free to vary in each epoch. The minimum electron Lorentz factor γ_{min}, particle distribution slope p, viewing angle θ, blackbody luminosity L_{bb} and blackbody temperature T_{bb} were tied. Asterisks mark parameters that were pegged to their limits. The statistic for the overall joint fit is χ^2/d.f. = 305.54/138 = 2.20 for model 1 and 284.45/123 = 2.31 for model 2. We also report the power P carried by the electrons, protons (assuming one cold proton per electron) and magnetic field, the total jet power $P_j = P_e + P_p + P_B$ and the equipartition fraction U_e/U_B.

Throughout this Article we adopt a standard Λ cold dark matter cosmology (where Λ is the cosmological constant) with $H_0 = 67.4$ km s^{-1} Mpc^{-1}, $\Omega_m = 0.315$ and $\Omega_\Lambda = 1 - \Omega_m = 0.685$ (ref. [52]). Using the cosmology calculator of ref. [53], AT 2022cmc's redshift of 1.193 corresponds to a luminosity distance of 8.45 Gpc. H_0, Hubble's constant; Ω_m, matter density; Ω_Λ, vacuum energy.

γ-rays and X-rays. Fermi/LAT. AT 2022cmc was not detected by Fermi/LAT (100 MeV to 10 GeV). During the 24 h period starting on 27 February 2022 UTC (that is, d 15–16 after discovery), the upper limits on the photon flux and the energy flux were 2.76×10^{-7} photons cm^{-2} s^{-1}, and 5.46×10^{-3} MeV cm^{-2} s^{-1}, respectively.

AstroSat/SXT. The AstroSat Soft X-ray Telescope (SXT; ref. [54]) observed AT 2022cmc on 23 February 2022 for an exposure time of 52.8 ks in the full-window mode. We processed the level-1 data using the SXT pipeline AS1SXTLevel2-1.4b available at the Payload Operation Center (POC) website (https://www.tifr.res.in/~astrosat_sxt/sxtpipeline.html) and generated the orbit-wise cleaned event files that were then merged using the SXTMerger tool (https://github.com/gulabd/SXTMerger.jl). We extracted the source spectrum and light curve using a circular region of radius 15 arcmin centred at the source position. The poor spatial resolution of the SXT spreads the source photons almost over the entire detector area, thus leaving no source-free regions for background spectral extraction. We therefore used a background spectrum that was generated by the POC from a large number of blank-sky observations. We used the redistribution matrix file available at the POC, and an updated ancillary response file. We grouped the spectral data to a minimum of 20 counts per bin, and analysed using the spectral fitting package XSPEC version 12.12.0[55]. We fitted the 0.7–8 keV SXT spectrum with a power-law model modified by the Galactic and host-galaxy absorption; that is, tbabs × ztbabs × zashift (powerlaw) in the XSPEC terminology. We fixed the Milky Way column at $N_{\mathrm{H,MW}} = 9 \times 10^{19}$ cm^{-2}, obtained from the HEASARC column-density calculator (https://heasarc.gsfc.nasa.gov/cgi-bin/Tools/w3nh/w3nh.pl)[56]. We also fixed the redshift at $z = 1.193$. This model resulted in an acceptable fit ($\chi^2 = 208.7$ for 231 d.f.) with $\Gamma = 1.63^{+0.15}_{-0.14}$, the host-galaxy absorption column of $2.9^{+3.2}_{-2.7} \times 10^{21}$ cm^{-2} and the absorption-corrected 0.7–8 keV flux of 4.3×10^{-12} erg s^{-1} cm^{-2}.

NICER. NICER started high-cadence monitoring (multiple visits per day) of AT 2022cmc on 16 February 2022 19:07:03 UTC or MJD 59626.80, roughly 5 d after optical discovery. The resultant dataset comprises several hundred snapshots (that is, good time intervals (GTIs)), whose exposures varied between a few hundred to roughly 1,200 s. In this work, we report data taken before MJD 59697 (28 April 2022); that is, from the first 76 d after optical discovery.

We started the NICER data analysis by downloading the raw, unfiltered (uf) data from the HEASARC public archive (https://heasarc.gsfc.nasa.gov/cgi-bin/W3Browse/w3browse.pl). We reprocessed the data using the standard procedures outlined on the NICER data analysis webpages (https://heasarc.gsfc.nasa.gov/docs/nicer/analysis_threads/). We followed the data reduction steps outlined in ref. [57].

NICER is a non-imaging instrument with a field-of-view area of roughly 30 arcmin^2 (radius of 3.1 arcmin). To test for the presence of potential contaminating sources in NICER's field of view, we extracted a 0.3–8 keV X-ray image using Swift/XRT observations of the field (Extended Data Fig. 1). We found that AT 2022cmc was the only source within NICER's field of view, implying that the flux from AT 2022cmc dominates the NICER light curve at all times.

We investigated the X-ray spectral evolution of AT 2022cmc by extracting time-resolved spectra from the NICER data taken between MJD 59626 and MJD 59642 at ~0.5 d intervals (Table 1). Spectral analysis from data beyond MJD 59642 (that is, where AT 2022cmc's flux was reduced and comparable to the NICER background) will be published in a separate work. The main steps we followed are described below.

1. First we extracted the combined unfiltered but calibrated (ufa) and cleaned (cl) event files using the start and the end times of all GTIs within a given epoch.
2. Then we used the 3c50 background model[58] on these combined ufa and cl files to estimate the average background and source spectra. All the detectors marked as 'hot' at least once in any of the individual GTIs were excluded. Hot detectors are those affected by optical light loading (see ref. [57] for more details). A detector is tagged as hot if its 0.0–0.2 keV raw count rate is more than 4σ above the median of all active (typically 52) NICER detectors.
3. Using the tools nicerarf and nicerrmf we extract an ancillary response file (arf) and redistribution matrix file (rmf) for each epoch.
4. Then we grouped the spectra using the optimal binning criterion described by ref. [59], also ensuring that each bin had at least 25 counts. We implemented this using the ftool ftgrouppha with grouptype = optmin and groupscale = 25.

We modelled the resulting time-resolved spectra in the 0.3–5.0 keV bandpass, the energy range in which the source was above the background using a tbabs × ztbabs × zashift (clumin*power-law) model in PyXspec, a Python implementation (https://heasarc.gsfc.nasa.gov/xanadu/xspec/python/html/index.html) of XSPEC[55]. We fixed the Milky Way column to $N_{\mathrm{H,MW}} = 9 \times 10^{19}$ cm^{-2}, estimated from the HEASARC nH calculator (https://heasarc.gsfc.nasa.gov/cgi-bin/Tools/w3nh/w3nh.pl)[56]. We tied the host-galaxy neutral hydrogen column to be the same across all the spectra and incorporated an additional 1% systematic uncertainty when fitting the data as recommended here: https://heasarc.gsfc.nasa.gov/docs/nicer/analysis_threads/cal-recommend/. The cosmological parameters were set in XSPEC to the values mentioned above. We set the E_{min} and the E_{max} parameters of clumin to 0.3 and 10.0, respectively, while the redshift was set to 1.193. This allowed us to compute the k-corrected, unabsorbed 0.3–10 keV luminosities at various epochs. A sample NICER X-ray spectrum is shown in Extended Data Fig. 2. We also tried a thermal model that resulted in strong systematic residuals throughout the X-ray bandpass considered, and hence we did not proceed any further with it.

The above modelling resulted in a total χ^2/d.f. of 2,135.3/1,956. The reduced χ^2 values are close to unity in all except epoch E21, during which systematic residuals below 1 keV and above 5 keV were clearly present. This epoch coincided with a hard (2–5 keV) X-ray flare. Multiple such flares are evident between MJD 59637 and 59697. One such flare was also captured by Swift (Fig. 1d). The spectro-timing analysis of these flares will be addressed in future work.

Following ref. [58], we set NICER's sensitivity limit to a conservative 0.3–5 keV count rate of 0.2 counts s^{-1} (normalized to 50 NICER detectors). In other words, any particular time segment in which the background-subtracted 0.3–5 keV count rate was less than 0.2 counts s^{-1} was treated as an upper limit of 7.4×10^{45} erg s^{-1}. This upper limit corresponded to a k-corrected 0.3–10 keV absorption-corrected luminosity of 1.2×10^{46} erg s^{-1} for a source at a redshift of 1.193 (Fig. 1a).

Swift/XRT. Swift was not operational during the optical detection of AT 2022cmc and the satellite resumed pointed operations on 17 February 2022[60]. Swift began monitoring AT 2022cmc on MJD 59633 (23 February 2022) and was observed under the ID of 00015023. The source was observed once a day between MJD 59633 and MJD 59638 and once every few days after MJD 59638. In this work, we used data until MJD 59703 (that is, observation IDs 00015023001 through 00015023035). We started our data analysis by downloading the raw, level-1 data from the HEASARC public archive and reprocessed them using the standard HEASoft tool xrtpipeline. Here we only considered the data taken in the photon-counting mode. We only used events with grades between 0 and 12 in the energy range of 0.3–5 keV to match NICER's bandpass. We extracted the source and background counts using a circular aperture of 47 arcsec and an annulus with an inner and outer radii of 80 arcsec and 200 arcsec, respectively. XRT count rates were extracted on a per-obsID basis and these values are provided in Supplementary Data 2.

To convert Swift/XRT count rates to fluxes, we extracted an average energy spectrum by combining all the XRT exposures. We fitted the 0.3–5.0 keV spectra with a power-law model, modified by AT 2022cmc's host-galaxy neutral hydrogen column and Milky Way, the same as the model used for the NICER data mentioned above. Because the signal-to-noise ratio of the Swift XRT spectrum is low, the host-galaxy hydrogen column was fixed at 9.8×10^{20} cm^{-2} as derived from NICER fits. We left the power-law photon index free, which yielded a best-fit value of 1.45 ± 0.06. This value was consistent with the NICER spectral fits. From this fit we estimated the observed 0.3–5 keV flux and a count rate-to-flux scaling factor of 3.6×10^{-11} erg cm^{-2} counts^{-1} to convert from the 0.3–5 keV background-subtracted XRT count rate to the observed flux in the 0.3–5 keV band (Fig. 2). The uncertainties on the count rates and, consequently, the scaled fluxes, were computed using the formulae for small number statistics described in ref. [61].

GRB and TDE comparison data. To compare the X-ray light curve of AT 2022cmc with other relativistic transients, we compiled a sample of X-ray light curves of the three known relativistic TDEs, together with the bright GRBs from ref. [62]. For the GRBs in our comparison sample, we downloaded the 0.3–10 keV count-rate light curves from the UK Swift Science Data Centre (UKSSDC)[63,64] and corrected them for absorption using the ratio of time-averaged unabsorbed flux to time-averaged observed flux per burst provided in the UKSSDC catalogue (https://www.swift.ac.uk/xrt_live_cat/). We k-corrected the light curves to rest-frame 0.3–10 keV luminosity following ref. [65], assuming a power-law spectrum with photon index given by the time-averaged photon-counting mode photon index from the UKSSDC catalogue.

We extracted X-ray light curves of the three relativistic TDEs using the UKSSDC XRT products builder (https://www.swift.ac.uk/user_objects/)[63,64]. We used a time bin size of 1 d. We converted the 0.3–10 keV count-rate light curves to unabsorbed flux using the counts-to-flux ratio of the time-averaged spectral fits, and k-corrected them to rest-frame 0.3–10 keV luminosity as described above. The X-ray spectral indices for Sw J1644+57 and Sw J2058+0516 varied between 1.2 and 1.8 (ref. [41]). This range is similar to AT 2022cmc (see Table 1). Here we used the following fiducial values: Sw J1644+57: counts:flux = 9.32×10^{-11} erg cm^{-2} count^{-1}, photon index = 1.58 ± 0.01; Sw J1112.2-8238: counts:flux = 6.13×10^{-11} erg cm^{-2} count^{-1}, photon index = 1.35 ± 0.08; Sw J2058.4+0516: counts:flux = 5.36×10^{-11} erg cm^{-2} count^{-1}, photon index = 1.55 ± 0.08. We plot these light curves, together with the GRB X-ray light curves extracted above, in Fig. 1.

UV/optical observations. ZTF. AT 2022cmc was discovered and reported by the ZTF[1] and released as a transient candidate ZTF22aaajecp in the public stream to brokers and the Transient Name Server, with data available in Lasair (https://lasair.roe.ac.uk/object/ZTF22aaajecp)[66]. We performed point spread function (PSF) photometry on all publicly available ZTF data using the ZTF forced-photometry service[67] in the g and r bands. We report our photometry corrected for Galactic extinction of $A_V = 0.0348$ mag (ref. [68]) and converted to flux density in millijansky. A_v is the total photometric extinction in the V (550 nm) band.

ATLAS. ATLAS (ref. [69]) is a 4 × 0.5 m telescope system that provides all-sky nightly cadence at typical limiting magnitudes of ~19.5 in cyan (g + r) and orange (r + i) filters. The data were processed in real time and the transients were identified by the ATLAS Transient Science Server[70]. We stacked individual nightly exposures and used the ATLAS forced-photometry server[71] to obtain the light curves of AT 2022cmc in both filters. Photometry was produced with standard PSF fitting techniques on the difference images and we initially reported the fast-declining optical flux in ref. [3].

Follow-up optical imaging. Follow-up observations of AT 2022cmc were conducted as part of the 'advanced' extended Public ESO Spectroscopic Survey of Transient Objects (ePESSTO+)[72] using the EFOSC2 imaging spectrograph at the ESO New Technology Telescope to obtain images in the g, r and i bands. Images were reduced using the custom PESSTO pipeline (https://github.com/svalenti/pessto), and the PSF photometry was measured without template subtraction using photometry-sans-frustration; an interactive Python wrapper that uses the Astropy and Photutils packages[73]. Aperture photometry was applied to the few images in which the target PSF was slightly elongated, otherwise the magnitudes were derived from PSF fitting. All photometry was calibrated against Pan-STARRS field stars.

AT 2022cmc was also followed up in the r, i, z and w bands with the 1.8 m Pan-STARRS2 telescope in Hawaii[74]. Pan-STARRS2 operates in survey mode, searching for near-Earth objects, but the survey can be interrupted for photometry of specific targets. Pan-STARRS2 is equipped with a 1.4 gigapixel camera with a pixel scale of 0.26 arcsec. The images were processed with the image processing pipeline[75] and difference imaging was performed using the PS1 Science Consortium [74] 3π survey data as reference. PSF photometry was used to compute instrumental magnitudes, and zero points were calculated from PS1 reference stars in the field.

AT 2022cmc was also observed as part of the Kinder (kilonova finder) survey[76] in the g, r and i bands with the 0.4 m SLT at Lulin Observatory, Taiwan. The images were reduced using a standard IRAF routine with bias, dark and flat calibrations. We used the automated photometry of transients pipeline[77] to perform PSF photometry and calibrate against SDSS field stars[78]. We used the Lulin one-metre telescope for deeper imaging in the g, r, i and z bands over four nights spanning 13.4–16.2 d post discovery. The images were also reduced using the standard charged-coupled device (CCD) processing techniques in IRAF. We performed aperture photometry calibrated against SDSS field stars. In a combined stack of the images from the Lulin one-metre telescope, AT 2022cmc was clearly detected in the g, r and i bands, with magnitudes of 21.76 ± 0.14, 21.71 ± 0.18 and 21.93 ± 0.31 mag, respectively, and undetected in the z band with an upper limit of >20.69 mag. We list the photometry from our individual observations in Supplementary Data 1.

We compiled additional optical photometry from the Gamma-ray Coordinates Network circulars[79–89] and corrected for extinction. These are also included in Supplementary Data 1.

Swift/UVOT. We performed photometry on Swift/UVOT[90] observations of AT 2022cmc with the uvotsource task in HEAsoft package v6.29 using a 5 arcsec aperture on the source position. Another region of 40 arcsec located at a nearby position was used to estimate the background emission. Because the host galaxy was not detected in the GALEX[91] co-added UV images and AT 2022cmc's UVOT detections are ~2 mag brighter then host upper limits (see 'Constraints on host luminosity'), we did not attempt any type of host subtraction.

AstroSat/Ultra-Violet Imaging Telescope. The AstroSat Ultra-Violet Imaging Telescope[92,93] onboard AstroSat[94] also observed the source, simultaneous with the SXT, with its far-UV channel using the F148W ($\lambda_{\rm mean} = 1{,}481$ Å; $\Delta\lambda = 500$ Å) and F154W ($\lambda_{\rm mean} = 1{,}541$ Å; $\Delta\lambda = 380$ Å) filters for exposures of 6,024 s and 9,674 s, respectively. We processed the level-1 data using the CCDLAB pipeline[95] and constructed broadband images. We extracted source counts using a circular aperture of radius 10 arcsec centred at the source position. We also extracted background counts from nearby source-free regions, and corrected for the background contribution. We then converted the net count rates to the flux densities using the flux conversion factors provided in refs. [92,93]. We did not detect the source, and obtained 3σ flux upper limits of 4.7×10^{-17} erg cm^{-2} s^{-1} Å^{-1} (F154W) and 6.4×10^{-17} erg cm^{-2} s^{-1} Å^{-1} (F148W).

Optical spectroscopy. We observed AT 2022cmc with the X-shooter spectrograph[96] on the ESO VLT on 27 February 2022. Data were obtained in on-slit nodding mode using the 1.0″, 0.9″ and 0.9″ slits in the UVB, Vis and near-infrared (NIR) arms respectively, with a spectral resolution of ~1 Å in the optical. We reduced the data following standard procedures[97]. We first removed cosmic rays with the tool astroscrappy (https://github.com/astropy/astroscrappy), which is based on the cosmic-ray removal algorithm in ref. [98]. Afterwards, we processed the data with the X-shooter pipeline v3.3.5 and the ESO workflow engine ESOReflex[99,100]. We reduced the UVB and Vis-arm data in stare mode to boost the signal to noise by a factor of $\sqrt{2}$ compared with the standard nodding mode reduction. We co-added the individual rectified and wavelength- and flux-calibrated two-dimensional spectra, followed by extraction of the one-dimensional spectra of each arm in a statistically optimal way using tools developed by J. Selsing (https://github.com/jselsing/XSGRB_reduction_scripts). Finally, we converted the wavelength calibration of all spectra to vacuum wavelengths and corrected the wavelength scale for barycentric motion. We stitched the spectra from the UVB and Vis arms by averaging in the overlap regions. We reduced the NIR data reduced in nodding mode to ensure a good sky-line subtraction. We did not detect a trace of the target in the NIR arm, and thus do not discuss the NIR data further.

The extracted spectrum consisted of a steep and largely featureless blue continuum, which we rebinned by 5 pixels to increase the signal-to-noise ratio (Extended Data Fig. 4). At the reported redshift $z = 1.193$, there is a hint of absorption features at wavelengths consistent with the Ca II H and K lines. The apparent absorption at ~2,600 Å was not a real feature, but instead a low-sensitivity, noisy region close to the edge of the UVB arm. The spectrum (covering approximately rest frame 1,500–4,500 Å) could be fitted well by a blackbody with $T \approx 30{,}000$ K, although a power law with $F_\nu \propto \nu^{0.6}$ also provided a satisfactory fit. The thermal model was preferred due to its consistency with the optical bump in the broadband SED (Fig. 3). This value was consistent with the measurement of ~2.3×10^4 K from the optical/UV SED, after accounting for the synchrotron contribution and the measurement uncertainty of ~10% on the value inferred from the VLT spectrum. This inferred temperature was similar to other optical TDEs[101].

Constraints on host luminosity. To derive upper limits on the luminosity of the host galaxy, we created deep reference images in the w, i and z bands by stacking Pan-STARRS1 and Pan-STARRS2 images of the field containing AT 2022cmc. These images were obtained during routine survey operations over a period spanning June 2010 to January 2022. The w band is a wide filter (3,900–8,500 Å) with an effective wavelength $\lambda_{\mathrm{eff}} \approx 6{,}000$ Å, and can thus be treated as the r band. The effective exposure times for the co-added reference stacks were 2,475 s, 13,700 s and 16,260 s in the w, i and z bands, respectively. The host galaxy of AT 2022cmc was not visible in any of these stacks, with upper limits of $w > 23.85$ mag, $i > 23.05$ mag and $z > 22.89$ mag (Extended Data Fig. 5).

The deepest observer-frame limit (r band) corresponded to a rest-frame absolute AB magnitude of $M_{2,740} > -19.9$, with a simple k-correction of $2.5\log(1+z)$ and the observer-frame central wavelength converted to rest-frame (approximately 2,740 Å), with only a Milky Way reddening correction applied to the observer-frame flux. The redder bands similarly corresponded to $M_{3,430} > -20.7$ and $M_{3950} > -20.8$. We performed similar analyses on GALEX[91] near-UV ($\lambda_{\mathrm{eff}} \approx 2{,}300$ Å) and far-UV ($\lambda_{\mathrm{eff}} \approx 1{,}535$ Å) filtered data by stacking all images that contained the position of AT 2022cmc. No underlying host emission was detected in any of stacked images, and the 3σ upper limits were >22.6 mag (near-UV) and >22.5 mag (far-UV).

Radio. VLA. We observed AT 2022cmc on 27 February 2022 (~15 d post discovery) with NSF VLA under programme 20B-377 (PI: K.D.A.). The observations were taken when the array was in its most extended A configuration. We used the C, X, Ku, K and Ka band receivers with the 3-bit digital samplers to obtain nearly continuous frequency coverage from 4 to 37 GHz. We used 3C286 for bandpass and flux density calibration. We used J1329+3154 for complex gain calibration at the K and Ka bands, and 3C286 otherwise. We reduced and imaged the data using standard procedures in the Common Astronomy Software Applications (CASA) v5.6.1-8[102]. We detect a bright unresolved point source at all frequencies, enabling us to split the data into 2 GHz bandwidth segments for photometry. The resulting SED is shown in Fig. 3.

AMI-LA. AMI-LA is a radio interferometer consisting of eight 12.8 m dishes with baselines from 18 to 110 m, located in Cambridge, UK[103]. AMI-LA observes at 15.5 GHz with a bandwidth of 5 GHz divided into 4,096 channels[104]. We observed AT 2022cmc with AMI-LA beginning 14.7 d post discovery[2]. We reduced the AMI-LA observations using a custom pipeline REDUCE_DC[105]. The pipeline averaged the data down to eight channels and performed flagging for radiofrequency interference and antenna shadowing. We used 3C286 for both amplitude and complex gain calibration. We performed additional flagging, imaging and deconvolution in CASA (v4.7.0). We combined the statistical uncertainty on the 15.5 GHz flux densities with a 5% systematic calibration uncertainty in quadrature. We detected an unresolved source with a flux density of 0.49 ± 0.03 mJy in the first epoch[106], and initiated subsequent observations at near-daily cadence. We present the full 15.5 GHz light curve in Fig. 2 and list the flux density measurements in Supplementary Data 1. We compiled additional radio measurements of AT 2022cmc reported online in Gamma-ray Coordinates Network circulars and Astronomer's Telegrams[79,107,108] together in Supplementary Data 1.

EVN sub-milliarcsecond position. We used the EVN to observe AT 2022cmc on 22–23 March 2022 (18:08–02:11 UTC), under project code RM017A (PI: J.C.A.M.-J.), making use of the real-time eVLBI mode. We observed in dual-polarization mode at a central frequency of 4.927 GHz. Our array consisted of 15 stations, with 10 standard EVN stations (Jodrell Bank Mk II, Effelsberg, Hartebeesthoek, the 16-m dishes at Irbene, Medicina, Noto, the 85′ dishes at Onsala, the 65-m dishes at Tianma, Torun and Yebes) that observed with a bandwidth of 256 MHz, and 5 stations from the eMERLIN array (Knockin, Darnhall, Pickmere, Defford and Cambridge), which observed with a reduced bandwidth of 64 MHz.

We processed the data through the EVN pipeline to derive the a priori amplitude calibration and bandpass corrections, and conducted further processing with the Astronomical Image Processing System (v.31DEC19[109]). We phase referenced the data on AT 2022cmc to the nearby (1.66° away) calibrator source J1329+3154, with an assumed position of (J2000) 13 h 29 min 52.864912 s, +31° 54′ 11.05446″. We detected AT 2022cmc as an unresolved point source with a significance of 6.4σ at a position of (J2000) 13 h 34 min 43.201308(6) s, +33° 13:00′ 6506(2)″. The quoted uncertainties (denoted in parentheses for the last significant digit) are purely statistical, with potential systematic errors (such as those from uncorrected tropospheric delay or clock errors) estimated to be at the level of ~0.07 mas.

Shortest X-ray variability timescale

Manual inspection of the 0.3–5 keV background-subtracted NICER light curve of AT 2022cmc (provided as a supplementary file as "allphot.txt") reveals multiple instances of a variation in the observed count rate by >50% within a span of a few hundred seconds. To quantify the variability timescale, we extracted an average power density spectrum (PDS) using uninterrupted exposures that were each 950 s long. Increasing the accumulation time to 1,024 s exposures yielded fewer samples (13, compared with 29) and only resulted in a marginal gain in low-frequency information from 1/950 Hz to 1/1,024 Hz) within the first month of discovery (that is, data acquired before MJD 59642; rapid flaring activity observed at later times will be considered in a separate work). To ensure minimal impact from background fluctuations, we considered only exposures that were above the background; that is, background-subtracted 0.3–5 keV count rates greater than 0.2 counts s^{-1} (normalized to 50 NICER detectors), close to the nominal limit described by ref. [58]. In addition to the standard filters described in 'γ-ray and X-rays/NICER' we imposed a filter to remove exposures where the observed mean 15–18 keV count rate was beyond 2σ of the median 15–18 keV rate measured across all exposures. This is an extra cautionary step to minimize the effect of background particle flaring, which is important for variability studies. This gave a total of 29 time series with a cumulative exposure of 27.55 ks (950 × 29). We computed a Leahy-normalized (ref. [110]; mean Poisson noise level of 2) average PDS sampled at 1/8 s from these time series (Extended Data Fig. 6). We found that the PDS was consistent with the Poisson noise level of 2 at high frequencies ($\gtrsim 10^{-2}$ Hz); however, the PDS started to rise above the noise level at $\lesssim 2 \times 10^{-3}$ Hz, and the lowest-frequency bin at 1/950 s is clearly well-above the noise level. This suggested that AT 2022cmc has systematic X-ray variability on timescales at least as short as ~1,000 s in the observer frame.

Arguments against a GRB afterglow

A potential association with the Fermi GRB 220211A[111] was ruled out by a more precise localization of that GRB[112]. Nevertheless, the early optical evolution resembled an off-axis gamma-ray burst GRB. Long GRBs occur as a result of the core collapse of massive stars (for example, refs. [113–115]). Their emission comes in two phases: prompt emission, which consists of high-energy γ-rays generated within the ultrarelativistic jet that is launched following collapse[116,117], and the afterglow, which is produced by shocks as the jet is decelerated in the environment surrounding the burst[118,119]. High-cadence NICER and Swift/XRT monitoring observations have shown that AT 2022cmc has been consistently brighter than even the most luminous known GRB afterglows by more than a factor of 10 (Fig. 1a). The most striking difference between AT 2022cmc and GRB afterglows is the persistence of rapid X-ray variability (for example, Fig. 1 and Extended Data Fig. 6). The NICER observations reveal short (~2.4 h observer frame, corresponding to ~1 h in the source rest frame) flares with increases in the count rate by factors of 2–10 that remain detectable until at least ~40 d post discovery. This variability requires that the X-ray emitting region be smaller than $R = 2\Gamma_j^2 c\delta t \approx 10^{-4}\,\Gamma_j^2$ pc. In contrast, the expected tangential radius of a GRB afterglow at a similar time is ~0.5 pc for typical parameters[120] and $\Gamma_j \lesssim 2$. Continued central engine activity, which operates at much smaller radii (~10^{13} cm, for example ref. [121]) may produce rapid variability[122], but even the longest GRBs (the so-called ultra-long class; ref. [123]) do not show signs of central engine activity beyond a day after trigger (for example ref. [124]). On the other hand, X-ray variability on timescales of tens of minutes has been inferred for the relativistic TDEs Sw J1644+57[125] and Sw J2058+05[126]. These properties strongly favour a non-GRB origin.

Multiwavelength SED modelling

Preliminary considerations. The full multiwavelength (radio to X-ray) SED of AT 2022cmc cannot be simply explained by synchrotron emission. To see this, we consider the SED at ~15.6 d post discovery (Extended Data Fig. 7) at radio (VLA), millimetre-band (GBT), UV (Swift/UVOT) and X-ray frequencies (NICER). The start and the end times of the GBT observation were MJD 59637.2868 and MJD 59637.2928. We found that the spectral index from the GBT millimetre-band (90 GHz) observation to the centre of the NICER X-ray band was $\beta_{\text{mm-X}} = -0.63 \pm 0.01$ (corresponding to $\nu F_\nu \propto \nu^{0.37}$). This was inconsistent with the observed hard NICER spectrum, $\beta_X = -0.40 \pm 0.02$ (corresponding to $\nu F_\nu \propto \nu^{0.60}$). Furthermore, the interpolation from the radio to the X-rays using the above spectral index overpredicted contemporaneous Swift/UVOT UM2-band observations (when corrected for Galactic extinction) by a factor of ~4. This is unlikely to be explained by UV variability, which seems to be $\lesssim$20% at this time. While extinction due to dust could suppress the UV flux, there is no evidence for substantial dust extinction along the line of sight, as evidenced by the blue $z' - g' \approx 0.1$ mag colour, as well as the blue optical spectrum at this time (see 'Optical spectroscopy'). The absence of substantial extinction was further confirmed by the HST F160W and F606W measurements at ~25.4 d, which yielded a spectral index of $\beta_{\text{F606–F160}} = 0.34 \pm 0.08$. Thus, it was not possible to extend a single power-law spectrum from the radio to the X-rays without a mismatch between the required spectral index and the observed X-ray spectral index, and without overpredicting the optical/UV flux, indicating that the radio and X-ray flux arise from distinct emission components at this time.

Furthermore, the optical SED at this time seems to peak in approximately the g band, with a spectral index $\beta_{g\text{–}um2} = -1.5 \pm 0.5$. This declining spectral index cannot connect with observed X-ray flux, as the spectral index between the optical and X-rays at this time is much harder, $\beta_{\text{opt-X}} \approx -0.2$. This suggests that the optical and X-ray emission at this time also arises from separate emission components. This is further confirmed by the very different temporal evolution in the X-rays ($\alpha_X \approx -2.2$ and optical ($\alpha_{r'} \approx -0.3$) at ~10–40 d post discovery.

The radio SED at $\lesssim$25 GHz was optically thick ($\beta \approx 2$), whereas the spectral index between the flux density measured with the VLA at 24.5 GHz and with the GBT at 90 GHz is $\beta_{\text{K-mm}} = -0.96 \pm 0.06$, indicating that a spectral break is present near the GBT frequency. A simple broken power-law fit to the radio-millimetre SED at this time with the post-break index fixed at $\beta \approx -1$ yielded a break frequency of $\nu_{\text{pk}} = 57.5 \pm 0.1$ GHz and a spectral peak flux density of $F_{\nu,pk} = 4.1 \pm 0.1$ mJy at 15.6 d. Identifying this as the peak of a synchrotron SED, a simple energy equipartition argument suggests a minimum kinetic energy of $E_{\text{K,iso}} \approx 10^{50}$ erg and radius of $R_{\text{eq}} \approx 10^{16}$ cm for this component[127]. In the next section, we relax the assumption of equipartition and perform a full model fit with a physical model including SSC emission in the X-rays and a blackbody component in the optical.

Model set-up. For our model fits, we created three SEDs of AT 2022cmc by combining the data taken on d 15–17, 25–27 and 41–46, as these epochs had the best multiwavelength coverage. In each of these SED epochs we had only single measurements in the optical, the UV filters and the various radio bands. However, multiple NICER/X-ray exposures were present. These were merged to extract combined spectra using the procedure outlined in 'NICER'. We fitted each SED with a simple homogeneous single-zone model, similar to those used for blazars, for example refs. [25–27]. In this model, a power-law energy distribution of electrons with number density n_e, energy index p, and minimum and maximum Lorentz factors γ_{min} and γ_{max} was injected in a spherical region of radius R, threaded with a magnetic field B and moving with a bulk Lorentz factor Γ_j with respect to the observer at viewing angle θ. The quantities B, n_e and R were calculated in the emitting region co-moving frame. We tested two different model set-ups to probe which radiative mechanisms were responsible for the high-energy emission. In the simplest case (which we call model 1), we considered synchrotron and SSC exclusively. In the second case, we tested a simple external inverse Compton model (model 2 from now on), in which the seed photons were provided by the optical blackbody component. Unlike ref. [128], we could not test whether the seed photons originated in the accretion disk, as this component was not detected in any of the SEDs we modelled and was therefore entirely unconstrained.

Modelling the UV/optical emission as, for example, a disk wind is very complex and beyond the scope of this work[40]. Given the thermal appearance of the UV/optical SED, we made the simplifying assumption that this was blackbody emission originating in a thin shell at a radius $R_{\text{bb}} = (L_{\text{bb}}/4\pi\sigma_{\text{sb}} T_{\text{bb}}^4)^{1/2}$ (in analogy with how blazar jet models typically treat the torus around the AGN, for example ref. [25]), and derived L_{bb} and

T_{bb} from the temperature and normalization of the thermal component as we ran the fit. To estimate the relative contribution of external Compton and SSC we needed to calculate the energy density in the co-moving frame of the jet. For this, we needed to assume an opening angle ϕ to convert the radius of emitting region R to a distance from the central engine. For simplicity, we took $\phi = 1/\Gamma_{\mathrm{j}}$ and estimated the distance from the black hole as $d = R/\phi = \Gamma_{\mathrm{j}}R$. Finally, we calculated the blackbody energy density U_{bb} as follows. For $d < R_{\mathrm{bb}}$, the emitting region in the jet is moving towards the blackbody (in which case external Compton is expected to contribute meaningfully to the SED) and we had simply $U_{\mathrm{bb}} = \Gamma_{\mathrm{j}}^2 L_{\mathrm{bb}}/(4\pi R_{\mathrm{bb}}^2 c)$. For $d \geq R_{\mathrm{bb}}$, we accounted self-consistently (following the prescription in ref. [129] for an AGN torus) for the deboosting of the photons, as the jet emitting region is moving away, rather than towards, the optical-emitting region. This choice of jet opening angle meant that the efficiency of external Compton was maximized with respect to SSC. This is because maximizing the jet opening angle (by setting $\phi = 1/\Gamma_{\mathrm{j}}$) minimized d for a given R, which in turn made it more likely that the optical photons would be Doppler-boosted in the frame of the jet. We note that for AGN jets, VLBI surveys find typical values of $\phi \approx 0.1\text{–}0.2\,\Gamma_{\mathrm{j}}$ (ref. [130]). This smaller opening angle would push the emitting region farther away from the blackbody, reducing the efficiency of external Compton. The cyclosynchrotron and inverse Compton emission were calculated using the Kariba libraries from the publicly available BHJet model[129].

We imported the data and model into the spectral fitting package ISIS v.1.6.2-51[131] and jointly fitted the SEDs at the three epochs. We tied γ_{min}, p, Γ_{j} and θ across all epochs (meaning that the parameters are free during the fit, but forced to be identical for each SED) and jointly fitted all three SEDs, aiming to simplify the parameter space as much as possible. To obtain a starting guess for the model parameters, we performed an uncertainty-weighted least-squares fit using the χ^2 statistic with the subplex minimization algorithm. We then explored the parameter space via Markov chain Monte Carlo with emcee[132] using 50 walkers for each free parameter (for a total of 900 walkers). We ran the Markov chain Monte Carlo for 15,000 steps and discarded the first 6,000 as 'burn-in'. We report the median and 1σ credible intervals (corresponding to 68% of the probability mass around the median) on each parameter, as well as additional derived quantities of interest, in Table 2. We present the model corresponding to the median values of the parameters in Fig. 3 and Extended Data Fig. 8 for models 1 and 2, respectively. We also show the 2D posterior distributions of the best-fitting parameters (for model 1) that exhibit some degeneracy in Extended Data Fig. 9.

Modelling results. In the case of model 1, we found that all the model parameters were well constrained by the data with minimal degeneracy, as is typical of single-zone models (for example refs. [28,133]). The constraints were weaker for model 2, but the model parameters remained fairly well determined. This behaviour can be understood as follows. The SED samples seven observable quantities: the synchrotron self-absorption frequency ν_t (set by the multiple radio points on the d 15–16 SED), the synchrotron luminosities in the optically thin and thick regimes $L_{\mathrm{s,thin}}$ and $L_{\mathrm{s,thick}}$ (constrained by the radio and optical data), the inverse Compton luminosity L_{ssc} (set by the NICER data), the X-ray photon index, the synchrotron scale frequency ν_{s} and the inverse Compton scale frequency ν_{c}. The free parameters in the model affected each observable quantity differently, and as a result it was possible to relate one to the other. For example, the bolometric synchrotron luminosity scales as $L_{\mathrm{s}} \propto n_{\mathrm{e}}R^3B^2\delta^4$, while the SSC bolometric luminosity scales as $L_{\mathrm{ssc}} \propto n_{\mathrm{e}}R^3\delta^4U_{\mathrm{s}}$, with $U_{\mathrm{s}} = L_{\mathrm{s}}/4\pi R^2c\delta^4$. As a result, $L_{\mathrm{ssc}} \propto n_{\mathrm{e}}^2B^2R^4\delta^4$, so that $L_{\mathrm{ssc}}/L_s \propto n_{\mathrm{e}}R$: for a fixed synchrotron luminosity, the large X-ray luminosity observed with NICER required a large number density and/or a large emitting region. In a similar fashion, B, n_{e}, R and δ were further constrained by the dependency of ν_{t}, $L_{\mathrm{s,thick}}$, ν_{s} and ν_{c} on the model parameters. The constraints on the remaining model parameters were more intuitive: p was determined by the slope of the X-ray spectra, because (to first order) a power-law electron distribution produces a power-law SSC spectrum with spectral index $\beta = (1 - p)/2$. Finally, once B and δ were determined, γ_{min} and γ_{max} were constrained by requiring that the synchrotron spectrum fell between the radio and optical frequency, and that the low-energy end of the SSC spectrum fell between UV and X-ray energies.

The main results of model 1 were as follows. First, we required the jet to be highly relativistic ($\Gamma_{\mathrm{j}} = 86^{+10}_{-9}$), viewed at a very small angle ($\theta \leq 1°$) and very powerful (~10^{46-47} erg s^{-1}, depending on the epoch and jet matter content). For comparison, this power was near or at the Eddington luminosity of a $10^8\,M_{\odot}$ black hole (roughly the largest black hole mass for which a main sequence star can be tidally disrupted). Second, the size of the emitting region was ~10^{15}–10^{16} cm, which was marginally consistent with the observed variability timescale of ~1,000 s owing to the strong beaming ($\delta \approx 100$). Finally, all of our best-fitting models required the energy density of the electrons ($U_{\mathrm{e}} = \langle\gamma\rangle n_{\mathrm{e}}m_{\mathrm{e}}c^2$, where $\langle\gamma\rangle$ is the average Lorentz factor of the radiating electrons) to be larger than that of the magnetic field ($U_B = B^2/8\pi$) by a factor of ~10^2 (up to 10^5 for d 25–27, although this number is probably driven by our choice of tying multiple parameters), implying that the bulk of the jet power is carried by the matter, rather than the magnetic field.

The picture is quite different in the case of model 2. First, this model required a small emitting region radius ($R \approx 10^{14}$ cm) and Γ_{j} (~5). This behaviour occurred because if external Compton was to contribute meaningfully to the SED, the emission had to originate close enough to the black hole that $d \leq R_{\mathrm{bb}}$, so that the external photons were Doppler boosted in the jet co-moving frame. Invoking a smaller emitting region resulted in larger estimates for B and n_{e}. In turn, this caused the synchrotron self-absorption frequency to move to ~10^{12} Hz, well above where the observed break lies in the data, and suppressing the predicted radio flux as a result. Consequently, the external Compton model predicted negligible radio flux, and the radio emission in this model must originate in a separate region. Requiring not one, but two, individual self-absorbing active regions in the jet meant that this external Compton model would require substantially more fine-tuning than the SSC model. We accounted for the inability of the external Compton model to reproduce the observed radio flux by neglecting the radio data entirely in the final model 2 fits (not doing so caused the fit to either recover the model 1 fits, or produce fits with χ^2/d.f. ≈ 70, rather than ~2.3 without the radio data). Neglecting the constraints provided by the self-absorbed synchrotron data also meant that the best-fitting parameters for model 2 were less well determined. Moreover, for seed blackbody photons peaking at $\nu_{\mathrm{bb}} \approx 10^{15}$ Hz the external Compton component only begins to be important at a frequency $\nu_{\mathrm{EC}} \approx \delta\Gamma_{\mathrm{j}}\gamma_{\mathrm{min}}^2\nu_{\mathrm{bb}} \approx 10^{18}$ Hz (ref. [28]). This scaling caused the external Compton component to only produce bright hard X-ray and/or soft γ-ray emission, while underpredicting the soft X-ray flux. Instead, at frequencies ≤10^{18} Hz the bulk of the flux was still produced through SSC, as in model 1. A similar behaviour was also found when modelling the SEDs of powerful blazars[25,26,30], in which the X-ray emission typically originates through SSC, while the γ-ray emission is dominated by external C. Similarly to model 1, producing a large soft X-ray flux through SSC required the jet to again be matter dominated, with $U_{\mathrm{e}}/U_{\mathrm{b}} \approx 100$. Finally, model 2 required smaller jet powers, with $P_{\mathrm{j}} \approx 10^{45}$ erg s^{-1}.

In summary, model 1 could satisfactorily fit the data at every epoch, although requiring a very highly beamed, matter-dominated jet. Model 2, on the other hand, greatly underpredicted the radio data, which instead required some fine-tuning in the form of a second self-absorbed emitting region farther downstream. While in this case the beaming requirements were less severe, a large SSC contribution was still required to match the X-ray flux, resulting in a similarly matter-dominated jet to model 1. Due to all these considerations, we favour model 1 over model 2, with the caveat that our treatment of the external Compton process is fairly simplistic. Despite this caveat, the models presented here provide strong evidence that the emission of AT 2022cmc originates in a relativistic jet pointed towards Earth.

Gravitational lens magnification by a foreground structure

The high luminosity of AT 2022cmc motivates considering whether gravitational lensing by a foreground structure along the line of sight has magnified the flux that we detected. AT 2022cmc is located 5.6 arcsec from the galaxy SDSS J133443.05 + 331305.7, at a photometric redshift of $z = 0.4 \pm 0.1$, and 3.7 arcmin from the galaxy group WHL J133453.9 + 331004 at a spectroscopic redshift of $z = 0.4$ (ref. [134]). The optical luminosity of the group, and the sky location and colours of this galaxy, are consistent with our line of sight to AT 2022cmc passing adjacent to a star-forming galaxy located in the infall region of ($R \simeq r_{200}$) of a galaxy group with a mass $M_{200} \simeq 3 \times 10^{13}\, M_{\odot}$, where the mass estimate was obtained by combining the optical luminosity from ref. [134] with the mass-observable scaling relations from ref. [135]. To estimate lens magnification by the group, we assumed an NFW density profile with concentration $c_{200} = 5$, and adopted the formalism from ref. [136] to estimate a magnification of $\mu \simeq 1.02$ (that is, just an approximately 2% magnification of the flux). To estimate magnification by the galaxy, we compared its apparent magnitude in red passbands (that is, relatively insensitive to any ongoing star formation) with a model for a passively evolving stellar population formed in a burst at a redshift of $z > 2$. This yielded an estimated luminosity relative to the luminosity function of cluster and group galaxies[137] of $\simeq 0.3\,_*$. Combining this estimate with the scaling relations between mass and luminosity commonly used to estimate galaxy masses in gravitational lens models (for example, ref. [138]) we obtained a velocity dispersion estimate for the bulge of the galaxy of $\sigma \simeq 120$ km s^{-1}. Then, adopting a singular isothermal sphere model of the galaxy mass distribution, and using the standard expressions for the lensing properties of a singular isothermal sphere (for example, ref. [139]), we derived an estimated Einstein radius of $\theta_{\rm E} \simeq 0.25$ arcsec and lens magnification of $\mu \simeq 1.05$, based on the lens redshift of $z_{\rm L} = 0.4$ and source redshift of $z_{\rm S} = 1.193$. In summary, the lens magnification suffered by AT 2022cmc seems to be modest at $\mu \simeq 1.05$–1.1, and cannot account for the high observed luminosity of the X-ray to radio counterpart.

Data availability

All the NICER and Swift data presented here are public and can be found in the NASA archives at: https://heasarc.gsfc.nasa.gov/cgi-bin/W3Browse/w3browse.pl. All the photometry presented in this work is available in Supplementary Data 1. Time-resolved NICER spectra can be downloaded from https://doi.org/10.5281/zenodo.6870587. Swift/XRT photometry is provided in Supplementary Data 2. The data presented in Table 1 are also available in a machine-readable format in Supplementary Data 3. Source data are provided with this paper.

Code availability

Please provide a code availability statement here.

References

1. Bellm, E. C. et al. The Zwicky Transient Facility: system overview, performance, and first results. *Publ. Astron. Soc. Pac.* **131**, 018002 (2019).
2. Andreoni, I. et al. ZTF22aaajecp/AT2022cmc: Zwicky Transient Facility discovery of a fast and red optical transient. *GRB Coord. Netw. Circ.* No. 31590 (2022).
3. Fulton, M. et al. ATLAS observations of the fast and red optical transient ZTF22aaajecp/AT2022cmc. *Transient Name Server AstroNote* 40 (2022).
4. Perley, D. A. ZTF22aaajecp/AT2022cmc: VLA radio detection. *GRB Coord. Netw. Circ.* No. 31592 (2022).
5. Ahumada, T. et al. ZTF22aaajecp/AT2022cmc: GMOS-N spectroscopy. *GRB Coord. Netw. Circ.* No. 31595 (2022).
6. Lundquist, M. J., Alvarez, C. A. & O'Meara, J. ZTF22aaajecp/AT2022cmc: Keck DEIMOS Redshift. *GRB Coord. Netw. Circ.* No. 31612 (2022).
7. Tanvir, N. R. et al. ZTF22aaajecp/AT2022cmc: VLT/X-shooter redshift. *GRB Coord. Netw. Circ.* No. 31602 (2022).
8. Pizzuto, A. et al. AT2022cmc/ZTF22aaajecpc: IceCube neutrino search. *The Astronomer's Telegram* 15239 (2022).
9. Pasham, D., Gendreau, K., Arzoumanian, Z. & Cenko, B. ZTF22aaajecp/AT2022cmc: NICER X-ray detection. *GRB Coord. Netw. Circ.* No. 31601 (2022).
10. Duran, R. B., Nakar, E. & Piran, T. Radius constraints and minimal equipartition energy of relativistically moving synchrotron sources. *Astrophys. J.* **772**, 78 (2013).
11. Rees, M. J. Tidal disruption of stars by black holes of 10^6–10^8 solar masses in nearby galaxies. *Nature* **333**, 523 (1988).
12. Bloom, J. S. et al. A possible relativistic jetted outburst from a massive black hole fed by a tidally disrupted star. *Science* **333**, 203 (2011).
13. Cenko, S. B. et al. Swift J2058.4+0516: discovery of a possible second relativistic tidal disruption flare? *Astrophys. J.* **753**, 77 (2012).
14. Pasham, D. R. et al. A multiwavelength study of the relativistic tidal disruption candidate Swift J2058.4+0516 at late times. *Astrophys. J.* **805**, 68 (2015).
15. Brown, G. C. et al. Swift J1112.2-8238: a candidate relativistic tidal disruption flare. *Mon. Not. R. Astron. Soc.* **452**, 4297 (2015).
16. van Velzen, S. et al. Seventeen tidal disruption events from the first half of ZTF survey observations: entering a new era of population studies. *Astrophys. J.* **908**, 4 (2021).
17. Wevers, T. et al. Evidence for rapid disc formation and reprocessing in the X-ray bright tidal disruption event candidate AT 2018fyk. *Mon. Not. R. Astron. Soc.* **488**, 4816 (2019).
18. Nicholl, M. et al. An outflow powers the optical rise of the nearby, fast-evolving tidal disruption event AT2019qiz. *Mon. Not. R. Astron. Soc.* **499**, 482 (2020).
19. Pasham, D. R. et al. Optical/UV-to-X-ray echoes from the tidal disruption flare ASASSN-14li. *Astrophys. J. Lett.* **837**, L30 (2017).
20. Piran, T., Svirski, G., Krolik, J., Cheng, R. M. & Shiokawa, H. Disk formation versus disk accretion—what powers tidal disruption events? *Astrophys. J.* **806**, 164 (2015).
21. Leloudas, G. et al. The superluminous transient ASASSN-15lh as a tidal disruption event from a Kerr black hole. *Nat. Astron.* **1**, 0002 (2016).
22. McClintock, J. E. & Remillard, R. A. in *Compact Stellar X-Ray Sources (Cambridge Astrophysics, Series No. 39)* Vol. 39 (eds Lewin, W & van der Klis, M.) 157–213 (Cambridge University Press, 2006).
23. Giannios, D. & Metzger, B. D. Radio transients from stellar tidal disruption by massive black holes. *Mon. Not. R. Astron. Soc.* **416**, 2102 (2011).
24. Romero, G. E., Boettcher, M., Markoff, S. & Tavecchio, F. Relativistic jets in active galactic nuclei and microquasars. *Space Sci. Rev.* **207**, 5 (2017).
25. Ghisellini, G. & Tavecchio, F. Canonical high-power blazars. *Mon. Not. R. Astron. Soc.* **397**, 985 (2009).
26. Böttcher, M., Reimer, A., Sweeney, K. & Prakash, A. Leptonic and hadronic modeling of Fermi-detected Blazars. *Astrophys. J.* **768**, 54 (2013).
27. Tavecchio, F. & Ghisellini, G. On the magnetization of BL Lac jets. *Mon. Not. R. Astron. Soc.* **456**, 2374 (2016).

28. Ghisellini, G. *Radiative Processes in High Energy Astrophysics, Lecture Notes in Physics* Vol. 873 (Springer International Publishing Switzerland, 2013).
29. Aharonian, F. et al. An exceptional very high energy gamma-ray flare of PKS 2155-304. *Astrophys. J. Lett.* **664**, L71 (2007).
30. Hayashida, M. et al. Rapid variability of blazar 3C 279 during flaring states in 2013-2014 with joint Fermi-LAT, NuSTAR, Swift, and ground-based multiwavelength observations. *Astrophys. J.* **807**, 79 (2015).
31. Raiteri, C. M. et al. Blazar spectral variability as explained by a twisted inhomogeneous jet. *Nature* **552**, 374 (2017).
32. McKinney, J. C. General relativistic magnetohydrodynamic simulations of the jet formation and large-scale propagation from black hole accretion systems. *Mon. Not. R. Astron. Soc.* **368**, 1561 (2006).
33. Chatterjee, K., Liska, M., Tchekhovskoy, A. & Markoff, S. B. Accelerating AGN jets to parsec scales using general relativistic MHD simulations. *Mon. Not. R. Astron. Soc.* **490**, 2200–2218 (2019).
34. Coughlin, E. R. & Begelman, M. C. Structured, relativistic jets driven by radiation. *Mon. Not. R. Astron. Soc.* **499**, 3158 (2020).
35. Bromberg, O. & Levinson, A. Hydrodynamic collimation of relativistic outflows: semianalytic solutions and application to gamma-ray bursts. *Astrophys. J.* **671**, 678 (2007).
36. Kohler, S., Begelman, M. C. & Beckwith, K. Recollimation boundary layers in relativistic jets. *Mon. Not. R. Astron. Soc.* **422**, 2282 (2012).
37. Coughlin, E. R. & Begelman, M. C. Hyperaccretion during tidal disruption events: weakly bound debris envelopes and jets. *Astrophys. J.* **781**, 82 (2014).
38. Costamante, L. et al. The NuSTAR view on hard-TeV BL Lacs. *Mon. Not. R. Astron. Soc.* **477**, 4257 (2018).
39. EHT MWL Science Working Groupet al. Broadband multi-wavelength properties of M87 during the 2017 Event Horizon Telescope campaign. *Astrophys. J. Lett.* **911**, L11 (2021).
40. Crumley, P. et al. Swift J1644+57: an ideal test bed of radiation mechanisms in a relativistic super-Eddington jet. *Mon. Not. R. Astron. Soc.* **460**, 396 (2016).
41. Seifina, E., Titarchuk, L. & Virgilli, E. Swift J164449.3+573451 and Swift J2058.4+0516: black hole mass estimates for tidal disruption event sources. *Astron. Astrophys.* **607**, A38 (2017).
42. Lu, W. & Kumar, P. External inverse-Compton emission from jetted tidal disruption events. *Mon. Not. R. Astron. Soc.* **458**, 1071 (2016).
43. Lacy, J. H., Townes, C. H. & Hollenbach, D. J. The nature of the central parsec of the Galaxy. *Astrophys. J.* **262**, 120 (1982).
44. Guillochon, J. & Ramirez-Ruiz, E. Hydrodynamical simulations to determine the feeding rate of black holes by the tidal disruption of stars: the importance of the impact parameter and stellar structure. *Astrophys. J.* **767**, 25 (2013).
45. Stone, N., Sari, R. & Loeb, A. Consequences of strong compression in tidal disruption events. *Mon. Not. R. Astron. Soc.* **435**, 1809 (2013).
46. Norman, S. M. J., Nixon, C. J. & Coughlin, E. R. Stars crushed by black holes. I. On the energy distribution of stellar debris in tidal disruption events. *Astrophys. J.* **923**, 184 (2021).
47. Coughlin, E. R. & Nixon, C. J. Partial stellar disruption by a supermassive black hole: is the light curve really proportional to $t^{-9/4}$? *Astrophys. J. Lett.* **883**, L17 (2019).
48. Nixon, C. J., Coughlin, E. R. & Miles, P. R. Partial, zombie, and full tidal disruption of stars by supermassive black holes. *Astrophys. J.* **922**, 168 (2021).
49. Golightly, E. C. A., Nixon, C. J. & Coughlin, E. R. On the diversity of fallback rates from tidal disruption events with accurate stellar structure. *Astrophys. J. Lett.* **882**, L26 (2019).
50. Hammerstein, E. et al. The final season reimagined: 30 tidal disruption events from the ZTF-I Survey. Preprint at https://arxiv.org/abs/2203.01461 (2022).
51. Bricman, K. & Gomboc, A. The prospects of observing tidal disruption events with the Large Synoptic Survey Telescope. *Astrophys. J.* **890**, 73 (2020).
52. Planck Collaborationet al. Planck 2018 results. VI. Cosmological parameters. *Astron. Astrophys.* **641**, A6 (2020).
53. Wright, E. L. A cosmology calculator for the world wide web. *Publ. Astron. Soc. Pac.* **118**, 1711 (2006).
54. Singh, K. P. et al. Soft X-ray focusing telescope aboard AstroSat: design, characteristics and performance. *J. Astrophys. Astron.* **38**, 29 (2017).
55. Arnaud, K. A. XSPEC: the first ten years. In *Astronomical Data Analysis Software and Systems V* Conference Series Vol. 101 (eds Jacoby, G. H. & Barnes, J.) 17 (Astronomical Society of the Pacific, 1996).
56. HI4PI Collaborationet al. HI4PI: A full-sky H I survey based on EBHIS and GASS. *Astron. Astrophys.* **594**, A116 (2016).
57. Pasham, D. R. et al. Evidence for a compact object in the aftermath of the extragalactic transient AT2018cow. *Nat. Astron.* **6**, 249 (2021).
58. Remillard, R. A. et al. An empirical background model for the NICER X-ray timing instrument. *Astron. J.* **163**, 130 (2022).
59. Kaastra, J. S. & Bleeker, J. A. M. Optimal binning of X-ray spectra and response matrix design. *Astron. Astrophys.* **587**, A151 (2016).
60. Cenko, B. Swift resumes pointed science observations. *GRB Coord. Netw. Circ.* No. 31603 (2022).
61. Gehrels, N. Confidence limits for small numbers of events in astrophysical data. *Astrophys. J.* **303**, 336 (1986).
62. Gompertz, B. P., Fruchter, A. S. & Pe'er, A. The environments of the most energetic gamma-ray bursts. *Astrophys. J.* **866**, 162 (2018).
63. Evans, P. A. et al. An online repository of Swift/XRT light curves of γ-ray bursts. *Astron. Astrophys.* **469**, 379 (2007).
64. Evans, P. A. et al. Methods and results of an automatic analysis of a complete sample of Swift-XRT observations of GRBs. *Mon. Not. R. Astron. Soc.* **397**, 1177 (2009).
65. Bloom, J. S., Frail, D. A. & Sari, R. The prompt energy release of gamma-ray bursts using a cosmological k-correction. *Astron. J.* **121**, 2879 (2001).
66. Smith, K. W. et al. Lasair: the transient alert broker for LSST:UK. *Res. Not. Am. Astron. Soc.* **3**, 26 (2019).
67. Masci, F. J. et al. The Zwicky Transient Facility: data processing, products, and archive. *Publ. Astron. Soc. Pac.* **131**, 018003 (2019).
68. Schlafly, E. F. & Finkbeiner, D. P. Measuring reddening with Sloan Digital Sky Survey stellar spectra and recalibrating SFD. *Astrophys. J.* **737**, 103 (2011).
69. Tonry, J. L. et al. ATLAS: a high-cadence all-sky survey system. *Publ. Astron. Soc. Pac.* **130**, 064505 (2018).
70. Smith, K. W. et al. Design and operation of the ATLAS Transient Science Server. *Publ. Astron. Soc. Pac.* **132**, 085002 (2020).
71. Shingles, L. et al. Release of the ATLAS forced photometry server for public use. *Transient Name Server AstroNote* 7 (2021).
72. Smartt, S. J. et al. PESSTO: survey description and products from the first data release by the Public ESO Spectroscopic Survey of Transient Objects. *Astron. Astrophys.* **579**, A40 (2015).
73. Nicholl, M. Photometry-sans-frustration: interactive python wrapper for point-spread fitting (psf) photometry. https://github.com/mnicholl/photometry-sans-frustration
74. Chambers, K. C. et al. The Pan-STARRS1 Surveys. Preprint at https://arxiv.org/abs/1612.05560 (2016).
75. Magnier, E. A. et al. Pan-STARRS pixel analysis: source detection and characterization. *Astrophys. J. Suppl. Ser.* **251**, 5 (2020).
76. Chen, T. W. et al. Kinder follow-up observations of AT 2021gca (ZTF21aapkbav). *Transient Name Server AstroNote* 92 (2021).

77. Brennan, S. J. & Fraser, M. The automated photometry of transients (AutoPhOT) pipeline. Preprint at https://arxiv.org/abs/2201.02635 (2022).
78. Chen, T. W. et al. Kinder follow-up observations of AT 2022cmc (ZTF22aaajecp). *Transient Name Server AstroNote* 39 (2022).
79. Perley, D. A. ZTF22aaajecp/AT2022cmc: VLA radio detection. *GRB Coord. Netw. Circ.* No. 31592 (2022).
80. Pankov, N. et al. ZTF22aaajecp/AT2022cmc: Zeiss-1000 of Koshka observatory optical observations. *GRB Coord. Netw. Circ.* No. 31593 (2022).
81. Perley, D. A. ZTF22aaajecp/AT2022cmc: Liverpool Telescope photometry. *GRB Coord. Netw. Circ.* No. 31594 (2022).
82. Kumar, H. et al. ZTF22aaajecp: GIT optical follow-up observations. *GRB Coord. Netw. Circ.* No. 31597 (2022).
83. Pankov, N. et al. ZTF22aaajecp/AT2022cmc: Terskol observatory optical observations. *GRB Coord. Netw. Circ.* No. 31625 (2022).
84. Freeburn, J. et al. ZTF22aaajecp/AT2022cmc: DECam photometry. *GRB Coord. Netw. Circ.* No. 31647 (2022).
85. Pankov, N. et al. ZTF22aaajecp/AT2022cmc: Mondy optical observations. *GRB Coord. Netw. Circ.* No. 31652 (2022).
86. Cenko, S. B., Andreoni, I. & Coughlin, M. ZTF22aaajecp/AT2022cmc: Hubble Space Telescope observations. *GRB Coord. Netw. Circ.* No. 31729 (2022).
87. Pankov, N. et al. ZTF22aaajecp/AT2022cmc: continued optical observations (Mondy, TSHAO, AbAO). *GRB Coord. Netw. Circ.* No. 31798 (2022).
88. Dimple, P. et al. ZTF22aaajecp/AT2022cmc: 1.3m DFOT optical observations. *GRB Coord. Netw. Circ.* No. 31805 (2022).
89. Pankov, N. et al. ZTF22aaajecp/AT2022cmc: continued optical observations (Mondy, SAO RAS, CrAO). *GRB Coord. Netw. Circ.* No. 31846 (2022).
90. Roming, P. W. A. et al. The Swift Ultra-Violet/Optical Telescope. *Space Sci. Rev.* **120**, 95 (2005).
91. Bianchi, L. et al. GALEX catalogs of UV sources: statistical properties and sample science applications: hot white dwarfs in the Milky Way. *Astrophys. Space Sci.* **335**, 161 (2011).
92. Tandon, S. N. et al. In-orbit calibrations of the ultraviolet imaging telescope. *Astron. J.* **154**, 128 (2017).
93. Tandon, S. N. et al. Additional calibration of the ultraviolet imaging telescope on board AstroSat. *Astron. J.* **159**, 158 (2020).
94. Singh, K. P. et al. ASTROSAT mission. In *Society of Photo-Optical Instrumentation Engineers (SPIE)* Conference Series Vol. 9144, 91441S (SPIE, 2014).
95. Postma, J. E. & Leahy, D. CCDLAB: a graphical user interface FITS image data reducer, viewer, and Canadian UVIT data pipeline. *Publ. Astron. Soc. Pac.* **129**, 115002 (2017).
96. Vernet, J. et al. X-shooter, the new wide band intermediate resolution spectrograph at the ESO Very Large Telescope. *Astron. Astrophys.* **536**, A105 (2011).
97. Selsing, J. et al. The X-shooter GRB afterglow legacy sample (XS-GRB). *Astron. Astrophys.* **623**, A92 (2019).
98. van Dokkum, P. G. Cosmic-ray rejection by Laplacian edge detection. *Publ. Astron. Soc. Pac.* **113**, 1420 (2001).
99. Goldoni, P. et al. Data reduction software of the X-shooter spectrograph. In *Society of Photo-Optical Instrumentation Engineers (SPIE)* Conference Series Vol. 6269 (eds McLean, I. S. & Iye, M.) 62692K (SPIE, 2006).
100. Modigliani, A. et al. The X-shooter pipeline. In *Observatory Operations: Strategies, Processes, and Systems III* Conference Series Vol. 7737 (eds Silva, D. R. et al.) 773728 (SPIE, 2010).
101. van Velzen, S. et al. Seventeen tidal disruption events from the first half of ZTF survey observations: entering a new era of population studies. *Astrophys. J.* **908**, 4 (2021).
102. McMullin, J. P., Waters, B., Schiebel, D., Young, W. & Golap, K. CASA architecture and applications. In *Astronomical Data Analysis Software and Systems XVI* Conference Series Vol. 376 (eds Shaw, R. A. et al.) p. 127 (Astronomical Society of the Pacific, 2007).
103. Zwart, J. T. et al. The Arcminute Microkelvin Imager. *Mon. Not. R. Astron. Soc.* **391**, 1545 (2008).
104. Hickish, J. et al. A digital correlator upgrade for the Arcminute MicroKelvin Imager. *Mon. Not. R. Astron. Soc.* **475**, 5677 (2018).
105. Anderson, G. E. et al. The Arcminute Microkelvin Imager catalogue of gamma-ray burst afterglows at 15.7 GHz. *Mon. Not. R. Astron. Soc.* **473**, 1512 (2018).
106. Sfaradi. I. et al. ZTF22aaajecp/AT2022cmc: AMI-LA radio detection. *GRB Coord. Netw. Circ.* No. 31667 (2022).
107. Dobie, D. et al. ZTF22aaajecp/AT2022cmc: ATCA detection. *GRB Coord. Netw. Circ.* No. 31665 (2022).
108. Alexander, K. et al. GBT/MUSTANG-2 90 GHz observations of AT2022cmc. *The Astronomer's Telegram* 15269 (2022).
109. Greisen, E. W. in *Information Handling in Astronomy – Historical Vistas*. Astrophysics and Space Science Library Vol. 285 (ed. Heck, A.) 109–125 (Springer, Dordrecht, 2003).
110. Leahy, D. A. et al. On searches for pulsed emission with application to four globular cluster X-ray sources : NGC 1851, 6441, 6624 and 6712. *Astrophys. J.* **266**, 160 (1983).
111. Fermi GBM Team. GRB 220211A: Fermi GBM final real-time localization. *GRB Coord. Netw. Circ.* No. 31570 (2022).
112. Ridnaia, A. et al. IPN triangulation of GRB 220211A (short). *GRB Coord. Netw. Circ.* No. 31584 (2022).
113. Woosley, S. E. Gamma-ray bursts from stellar mass accretion disks around black holes. *Astrophys. J.* **405**, 273 (1993).
114. MacFadyen, A. I. & Woosley, S. E. Collapsars: gamma-ray bursts and explosions in "failed supernovae". *Astrophys. J.* **524**, 262 (1999).
115. Kumar, P. & Zhang, B. The physics of gamma-ray bursts & relativistic jets. *Phys. Rep.* **561**, 1 (2015).
116. Blandford, R. D. & McKee, C. F. Fluid dynamics of relativistic blast waves. *Phys. Fluids* **19**, 1130 (1976).
117. Paczynski, B. Gamma-ray bursters at cosmological distances. *Astrophys. J. Lett.* **308**, L43 (1986).
118. Rees, M. J. & Meszaros, P. Relativistic fireballs - energy conversion and time-scales. *Mon. Not. R. Astron. Soc.* **258**, 41 (1992).
119. Sari, R., Piran, T. & Narayan, R. Spectra and light curves of gamma-ray burst afterglows. *Astrophys. J. Lett.* **497**, L17 (1998).
120. Granot, J. & Sari, R. The shape of spectral breaks in gamma-ray burst afterglows. *Astrophys. J.* **568**, 820 (2002).
121. Pe'er, A. Physics of gamma-ray bursts prompt emission. *Adv. Astron.* **2015**, 907321 (2015).
122. Kobayashi, S., Piran, T. & Sari, R. Can internal shocks produce the variability in gamma-ray bursts? *Astrophys. J.* **490**, 92 (1997).
123. Levan, A. J. et al. A new population of ultra-long duration gamma-ray bursts. *Astrophys. J.* **781**, 13 (2014).
124. Zhang, B.-B., Zhang, B., Murase, K., Connaughton, V. & Briggs, M. S. How long does a burst burst? *Astrophys. J.* **787**, 66 (2014).
125. Saxton, C. J., Soria, R., Wu, K. & Kuin, N. P. M. Long-term X-ray variability of Swift J1644+57. *Mon. Not. R. Astron. Soc.* **422**, 1625 (2012).
126. Pasham, D. R. et al. A multiwavelength study of the relativistic tidal disruption candidate Swift J2058.4+0516 at late times. *Astrophys. J.* **805**, 68 (2015).
127. Duran, R. B., Nakar, E. & Piran, T. Radius constraints and minimal equipartition energy of relativistically moving synchrotron sources. *Astrophys. J.* **772**, 78 (2013).
128. Burrows, D. N. et al. Relativistic jet activity from the tidal disruption of a star by a massive black hole. *Nature* **476**, 421 (2011).

129. Lucchini, M. et al. Bhjet: a public multi-zone, steady state jet + thermal corona spectral model. *MNRAS* https://doi.org/10.1093/mnras/stac2904 (2022).
130. Pushkarev, A. B., Kovalev, Y. Y., Lister, M. L. & Savolainen, T. Jet opening angles and gamma-ray brightness of AGN. *Astron. Astrophys.* **507**, L33 (2009).
131. Houck, J. C. & Denicola, L. A. ISIS: an interactive spectral interpretation system for high resolution X-ray spectroscopy. In *Astronomical Data Analysis Software and Systems IX* Conference Series Vol. 216 (eds Manset, N. et al.) 591 (Astronomical Society of the Pacific, 2000).
132. Foreman-Mackey, D., Hogg, D. W., Lang, D. & Goodman, J. emcee: the MCMC hammer. *Publ. Astron. Soc. Pac.* **125**, 306 (2013).
133. Tavecchio, F., Maraschi, L. & Ghisellini, G. Constraints on the physical parameters of TeV blazars. *Astrophys. J.* **509**, 608 (1998).
134. Wen, Z. L. & Han, J. L. Calibration of the optical mass proxy for clusters of galaxies and an update of the WHL12 cluster catalog. *Astrophys. J.* **807**, 178 (2015).
135. Mulroy, S. L. et al. LoCuSS: scaling relations between galaxy cluster mass, gas, and stellar content. *Mon. Not. R. Astron. Soc.* **484**, 60 (2019).
136. Wright, C. O. & Brainerd, T. G. Gravitational lensing by NFW halos. *Astrophys. J.* **534**, 34 (2000).
137. Lin, Y.-T., Mohr, J. J. & Stanford, S. A. K-band properties of galaxy clusters and groups: luminosity function, radial distribution, and halo occupation number. *Astrophys. J.* **610**, 745 (2004).
138. Richard, J. et al. LoCuSS: first results from strong-lensing analysis of 20 massive galaxy clusters at z = 0.2. *Mon. Not. R. Astron. Soc.* **404**, 325 (2010).
139. Smith, G. P. et al. Discovering gravitationally lensed gravitational waves: predicted rates, candidate selection, and localization with the Vera Rubin Observatory. Preprint at https://arxiv.org/abs/2204.12977 (2022).

Acknowledgements

D.R.P. would like to thank S. Dicker for sharing details of the GBT observations. D.R.P. was supported by NASA grant number 80NSSC22K0961 for this work. S.J.B. would like to thank Science Foundation Ireland and the Royal Society (grant number RS-EA/3471) for their support. S. Schulze acknowledges support from the G.R.E.A.T. research environment, funded by *Vetenskapsrådet*, the Swedish Research Council, under project number 2016-06012. F.O. acknowledges support from MIUR, PRIN 2017 (grant number 20179ZF5KS) "The new frontier of the Multi-Messenger Astrophysics: follow-up of electromagnetic transient counterparts of gravitational wave sources" and the support of HORIZON2020: AHEAD2020 grant agreement number 871158. G.L. and P.C. were supported by a research grant (number 19054) from VILLUM FONDEN. N.C.S. acknowledges support from the Science and Technology Facilities Council (STFC), and from STFC grant number ST/M001326/. M.N., B.P.G., A.A., E.J.R. and X.S. are supported by the European Research Council (ERC) under the European Union's Horizon 2020 research and innovation programme (grant agreement number 948381). L.R. acknowledges the support given by the Science and Technology Facilities Council through an STFC studentship. T.L. acknowledges support from the Radboud Excellence Initiative. T.M.B. acknowledges financial support from the Spanish Ministerio de Ciencia e Innovación (MCIN), the Agencia Estatal de Investigación (AEI) 10.13039501100011033 under the PID2020-115253GA-I00 HOSTFLOWS project, from Centro Superior de Investigaciones Científicas (CSIC) under the PIE project 20215AT016 and the I-LINK 2021 LINKA20409 and the programme Unidad de Excelencia María de Maeztu CEX2020-001058-M. C.-C.N. thanks the Ministry of Science and Technology (Taiwan) for funding under the contract 109-2112-M-008-014-MY3. M.P.T. acknowledges financial support from the State Agency for Research of the Spanish MCIU through the "Center of Excellence Severo Ochoa" award to the Instituto de Astrofísica de Andalucía (SEV-2017-0709) and through the grant PID2020-117404GB-C21 (MCI/AEI/FEDER, UE). Support for A.C. was provided by ANID through grant number ICN12_12009 awarded to the Millennium Institute of Astrophysics (MAS) and by ANID's Basal projects AFB-170002 and FB210003. E.R.C. acknowledges support from the National Science Foundation through grant number AST-2006684, and a Ralph E. Powe Junior Faculty Enhancement Award through the Oakridge Associated Universities. Pan-STARRS is a project of the Institute for Astronomy of the University of Hawaii, and is supported by the NASA SSO Near Earth Observation Program under grant numbers 80NSSC18K0971, NNX14AM74G, NNX12AR65G, NNX13AQ47G, NNX08AR22G and 80NSSC21K1572 and by the State of Hawaii. This publication has made use of data collected at Lulin Observatory, partly supported by MoST grant number 108-2112-M-008-001. We thank Lulin staff H.-Y. Hsiao, C.-S. Lin, W.-J. Hou and J.-K. Guo for observations and data management. This work was supported by the Australian government through the Australian Research Council's Discovery Projects funding scheme (DP200102471). The Pan-STARRS1 Surveys (PS1) and the PS1 public science archive have been made possible through contributions by the Institute for Astronomy, the University of Hawaii, the Pan-STARRS Project Office, the Max-Planck Society and its participating institutes, the Max Planck Institute for Astronomy, Heidelberg, and the Max Planck Institute for Extraterrestrial Physics, Garching, The Johns Hopkins University, Durham University, the University of Edinburgh, Queen's University Belfast, the Harvard-Smithsonian Center for Astrophysics, the Las Cumbres Observatory Global Telescope Network Incorporated, the National Central University of Taiwan, the Space Telescope Science Institute, the National Aeronautics and Space Administration under grant number NNX08AR22G issued through the Planetary Science Division of the NASA Science Mission Directorate, the National Science Foundation grant number AST-1238877, the University of Maryland, Eotvos Lorand University (ELTE), the Los Alamos National Laboratory and the Gordon and Betty Moore Foundation. R.R. and D.R.P. acknowledge partial support from the NASA grant number 80NSSC19K1287, for contributions to NICER. The European VLBI Network is a joint facility of independent European, African, Asian, and North American radio astronomy institutes. Scientific results from data presented in this publication are derived from EVN project code RM017A. e-VLBI research infrastructure in Europe is supported by the European Union's Seventh Framework Programme (FP7/2007-2013) under grant agreement number RI-261525 NEXPReS. A.H. is grateful for support by the I-Core Program of the Planning and Budgeting Committee and the Israel Science Foundation, and support under ISF grant number 647/18. This research was supported by grant number 2018154 from the United States-Israel Binational Science Foundation (BSF). We acknowledge the staff who operate and run the AMI-LA telescope at Lord's Bridge, Cambridge, for the AMI-LA radio data. AMI is supported by the Universities of Cambridge and Oxford, and by the European Research Council under grant number ERC-2012-StG-307215 LODESTONE. NICER is a 0.2–12 keV X-ray telescope operating on the International Space Station. The NICER mission and portions of the NICER science team activities are funded by NASA. The AstroSat mission is operated by the Indian Space Research Organisation (ISRO), the data are archived at the Indian Space Science Data Centre (ISSDC). The SXT data-processing software is provided by the Tata Institute of Fundamental Research (TIFR), Mumbai, India. The UVIT data were checked and verified by the UVIT POC at IIA, Bangalore, India. M.G. is supported by the EU Horizon 2020 research and innovation programme under grant agreement number 101004719. L.S. acknowledges support by the European Research Council (ERC) under the European Union's Horizon 2020 research and innovation programme (ERC Advanced Grant KILONOVA number 885281). M.P.T. acknowledges financial support from the State Agency for Research of the Spanish MCIU through the "Center of Excellence Severo Ochoa" award to the Instituto de Astrofísica de Andalucía (grant number SEV-2017-0709) and through grant number PID2020-117404GB-C21 (MCI/AEI/FEDER, UE). Support for this work was provided by NASA through the Smithsonian Astrophysical Observatory (SAO) contract number SV3-73016 to MIT for Support of the Chandra X-Ray Center (CXC) and Science Instruments. S.Y. has been supported by the research project grant "Understanding the Dynamic Universe" funded by the Knut and Alice Wallenberg Foundation under Dnr KAW 2018.0067, and the G.R.E.A.T research environment, funded by *Vetenskapsrådet*, the Swedish Research Council, project number 2016-06012. S.J.S., SS and K.W.S. acknowledge funding from STFC grant numbers ST/T000198/1 and ST/S006109/1. I.A. is a CIFAR Azrieli Global Scholar in the Gravity and the Extreme Universe Program and acknowledges support from that programme, from the European Research Council (ERC) under the European Union's Horizon 2020 research and innovation programme (grant agreement number 852097), from the Israel Science Foundation (grant number 2752/19), from the United States–Israel Binational Science Foundation (BSF), and from the Israeli Council for Higher Education Alon Fellowship. E.F. is supported by NASA under award number 80GSFC21M0002. The National Radio Astronomy Observatory is a facility of the National Science Foundation operated under cooperative agreement by Associated Universities, Inc. G.P.S. acknowledges support from The Royal Society, the Leverhulme Trust and the Science and Technology Facilities Council (grant numbers ST/N021702/1 and ST/S006141/1). L.G. acknowledges financial support from the Spanish Ministerio de Ciencia e Innovación (MCIN), the Agencia Estatal de Investigación (AEI) 10.13039/501100011033, and the European Social Fund (ESF) "Investing in your future" under the 2019 Ramón y Cajal programme RYC2019-027683-I and the PID2020-115253GA-I00 HOSTFLOWS project, from Centro Superior de Investigaciones Científicas (CSIC) under the PIE project 20215AT016 and the programme Unidad de Excelencia María de Maeztu CEX2020-001058-M. ECF is supported by NASA under award number 80GSFC21M0002. This work was completed in part using the Discovery cluster, supported by Northeastern University's Research Computing team.

Author contributions

D.R.P. led the overall project, acquired X-ray data, performed the reduction and wrote a large portion of the paper. M.L. performed SED modelling and the subsequent interpretation, and wrote part of the paper. T.L. aided in the interpretation and writing of the paper. B.P.G., S.S., M.N., S.J.S. and M.F acquired optical data and wrote part of the paper. K.G. and E.F. carried out the NICER X-ray observations. G.D. and P.R. acquired and reduced AstroSat data. G.P.S wrote the discussion about gravitational lensing. J.C.A.M.-J., K.D.A., S.v.V., T.L. and A.G. acquired the radio data, performed their reduction and contributed towards the writing of the manuscript. L.R., A.H., I.S. and R.F provided the AMI/radio data and wrote part of the paper. M.G. reduced optical data and wrote part of the paper. N.C.S., A.A., J.P.A., I.A., S.J.B., K.C., P.C., T.-W.C., A.C., T.d.B., M.D., L.G., H.G., J.H.G., M.G., M.H., P.G.J., E.K., T.L.K, P.K., G.L., C.-C.L., R.M., S.O., F.O., Y.-C.P., M.P.T., R.R., E.J.R., S.S., X.S., L.S., K.W.S., J.S., R.W., T.W. and S.Y. facilitated the discussion and contributed to the interpretation of the results. D.K. computed the Fermi upper limits. M.J. aided in SED modelling. C.-C.N., E.R.C., S.M., T.M. and T.M.-B contributed towards the data and interpretation.

Competing interests

The authors declare no competing interests.

Additional information

Extended data is available for this paper at https://doi.org/10.1038/s41550-022-01820-x.

Supplementary information The online version contains supplementary material available at https://doi.org/10.1038/s41550-022-01820-x.

Correspondence and requests for materials should be addressed to Dheeraj R. Pasham.

Peer review information *Nature Astronomy* thanks the anonymous reviewers for their contribution to the peer review of this work.

Reprints and permissions information is available at www.nature.com/reprints.

Dheeraj R. Pasham[1]✉, Matteo Lucchini[1], Tanmoy Laskar[2], Benjamin P. Gompertz[3,4], Shubham Srivastav[5], Matt Nicholl[3,4], Stephen J. Smartt[5], James C. A. Miller-Jones[6], Kate D. Alexander[7], Rob Fender[8], Graham P. Smith[4], M. Fulton[5], Gulab Dewangan[9], Keith Gendreau[10], Eric R. Coughlin[11], Lauren Rhodes[8], Assaf Horesh[12], Sjoert van Velzen[13], Itai Sfaradi[12], Muryel Guolo[14], Noel Castro Segura[15], Aysha Aamer[3,4], Joseph P. Anderson[16], Iair Arcavi[17,18], Seán J. Brennan[19], Kenneth Chambers[20], Panos Charalampopoulos[21], Ting-Wan Chen[22], A. Clocchiatti[23,24], Thomas de Boer[20], Michel Dennefeld[25], Elizabeth Ferrara[10,26,27], Lluís Galbany[28,29], Hua Gao[20], James H. Gillanders[5], Adelle Goodwin[6], Mariusz Gromadzki[30], M. Huber[20], Peter G. Jonker[2,31], Manasvita Joshi[32], Erin Kara[1], Thomas L. Killestein[33], Peter Kosec[1], Daniel Kocevski[34], Giorgos Leloudas[21], Chien-Cheng Lin[20], Raffaella Margutti[35], Seppo Mattila[36,37], Thomas Moore[5], Tomás Müller-Bravo[28,29], Chow-Choong Ngeow[38], Samantha Oates[3,4], Francesca Onori[39], Yen-Chen Pan[38], Miguel Perez-Torres[37,40,41], Priyanka Rani[9], Ronald Remillard[1], Evan J. Ridley[3,4], Steve Schulze[22], Xinyue Sheng[3,4], Luke Shingles[42], Ken W. Smith[5], James F. Steiner[43], Richard Wainscoat[20], Thomas Wevers[16] & Sheng Yang[22]

[1]Kavli Institute for Astrophysics and Space Research, Massachusetts Institute of Technology, Cambridge, MA, USA. [2]Department of Astrophysics/IMAPP, Radboud University, PO Box 9010, Nijmegen, The Netherlands. [3]Institute of Gravitational Wave Astronomy, University of Birmingham, Birmingham, UK. [4]School of Physics and Astronomy, University of Birmingham, Birmingham, UK. [5]Astrophysics Research Centre, School of Mathematics and Physics, Queen's University Belfast, Belfast, UK. [6]International Centre for Radio Astronomy Research, Curtin University, GPO Box U1987, Perth, WA, Australia. [7]Center for Interdisciplinary Exploration and Research in Astrophysics (CIERA) and Department of Physics and Astronomy, Northwestern University, 1800 Sherman Ave, Evanston, IL, USA. [8]Astrophysics, Department of Physics, University of Oxford, Keble Road, Oxford, UK. [9]The Inter-University Centre for Astronomy and Astrophysics, Pune, India. [10]NASA Goddard Space Flight Center, Greenbelt, MD, USA. [11]Department of Physics, Syracuse University, Syracuse, New York, USA. [12]Racah Institute of Physics, The Hebrew University of Jerusalem, Jerusalem, Israel. [13]Leiden Observatory, Leiden University, Postbus 9513, Leiden, The Netherlands. [14]Department of Physics and Astronomy, Johns Hopkins University, 3400 N. Charles St., Baltimore, MD, USA. [15]Department of Physics & Astronomy, University of Southampton, Southampton, UK. [16]European Southern Observatory, Alonso de Córdova 3107, Casilla 19, Santiago, Chile. [17]The School of Physics and Astronomy, Tel Aviv University, Tel Aviv, Israel. [18]CIFAR Azrieli Global Scholars program, CIFAR, Toronto, Canada. [19]School of Physics, O'Brien Centre for Science North, University College Dublin, Belfield Dublin 4, Ireland. [20]Institute for Astronomy, University of Hawaii, Honolulu, Hawaii, USA. [21]DTU Space, National Space Institute, Technical University of Denmark, Elektrovej 327, Lyngby, Denmark. [22]The Oskar Klein Centre, Department of Astronomy, Stockholm University, AlbaNova, Stockholm, Sweden. [23]Instituto de Astrofísica, Pontificia Universidad Católica, Vicuña Mackenna 4860, Santiago, Chile. [24]Millennium Institute of Astrophysics, Nuncio Monseñor Sótero Sanz 100, Of. 104, Providencia, Santiago, Chile. [25]IAP/Paris & Sorbonne Universities, Paris, France. [26]Center for Exploration and Space Studies (CRESST), Greenbelt, USA. [27]Department of Astronomy, University of Maryland, College Park, USA. [28]Institute of Space Sciences (ICE, CSIC), Campus UAB, Carrer de Can Magrans, s/n, Barcelona, Spain. [29]Institut d'Estudis Espacials de Catalunya (IEEC), Barcelona, Spain. [30]Astronomical Observatory, University of Warsaw, Al. Ujazdowskie 4, Warszawa, Poland. [31]SRON, Netherlands Institute for Space Research, Niels Bohrweg 4, Leiden, The Netherlands. [32]Research Computing, ITS Division, Northeastern University, Boston, MA, USA. [33]Department of Physics, University of Warwick, Gibbet Hill Road, Coventry, UK. [34]NASA Marshall Space Flight Center, Huntsville, AL, USA. [35]Department of Astronomy, University of California, 501 Campbell Hall, Berkeley, CA, USA. [36]Tuorla Observatory, Department of Physics and Astronomy, University of Turku, Turku, Finland. [37]School of Sciences, European University Cyprus, Diogenes Street, Engomi, Nicosia, Cyprus. [38]Graduate Institute of Astronomy, National Central University, Jhongli, Taiwan. [39]INAF-Osservatorio Astronomico d'Abruzzo, , via M. Maggini snc, Teramo, Italy. [40]Instituto de Astrofísica de Andalucía (IAA-CSIC), Glorieta de la Astronomía s/n, Granada, Spain. [41]Facultad de Ciencias, Universidad de Zaragoza, Pedro Cerbuna 12, Zaragoza, Spain. [42]GSI Helmholtzzentrum für Schwerionenforschung, Planckstraße 1, Darmstadt, Germany. [43]Smithsonian Astrophysical Observatory, 60 Garden Street, Cambridge, MA 02138, USA. ✉e-mail: drreddy@mit.edu

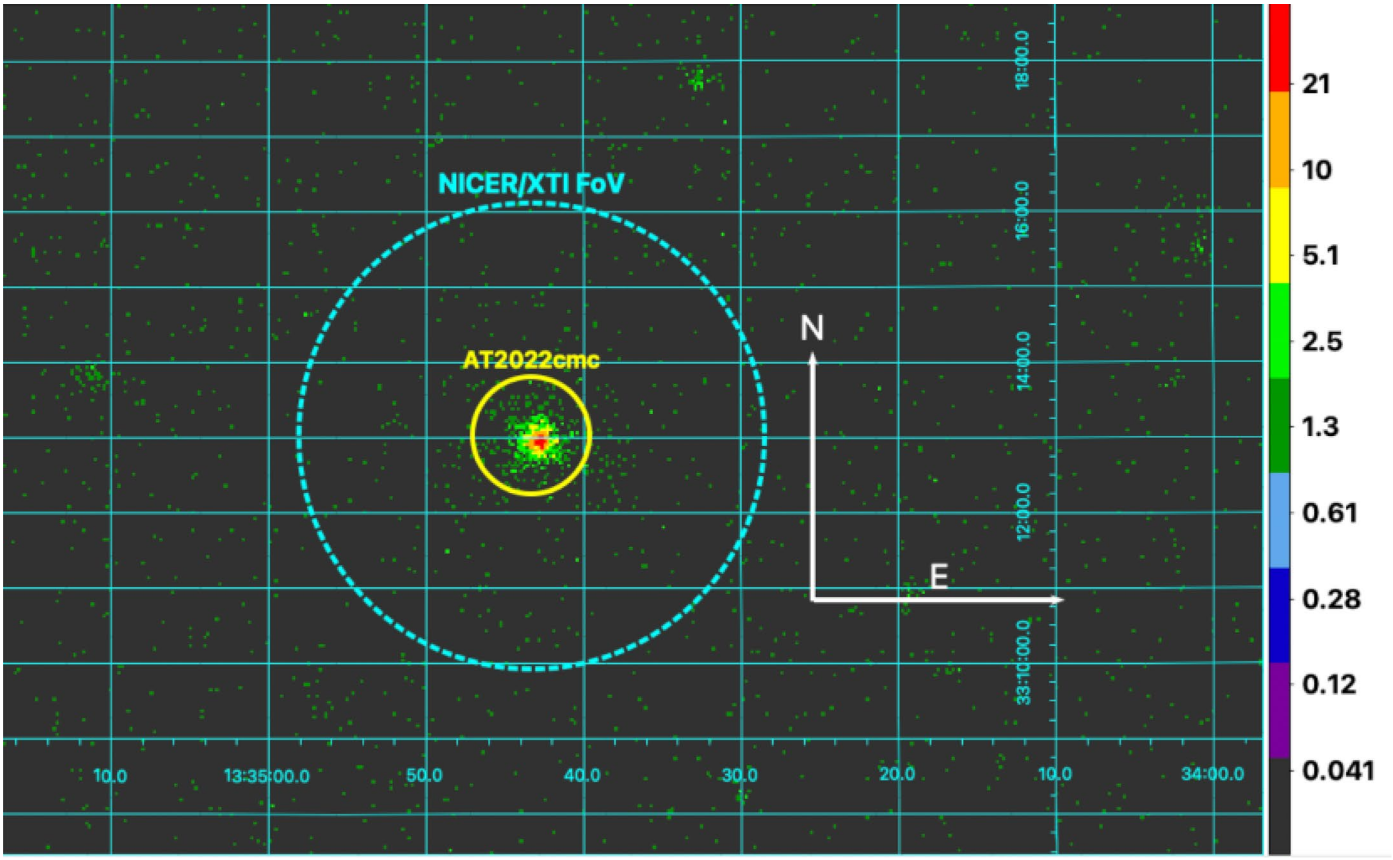

Extended Data Fig. 1 | Neil Gehrels Swift XRT 0.3-8 keV image of NICER's FoV. The yellow circle with a radius of 47″ and is centered on AT 2022cmc's radio coordinates of 13:34:43.2, +33:13:00.6 (J2000.0 epoch). The outer/dashed cyan circle shows NICE /XTI's approximate field of view of 3.1′ radius. There are no contaminating sources within NICER's FoV. The north and east arrows are each 200′ long. The color bar shows the number of X-ray counts.

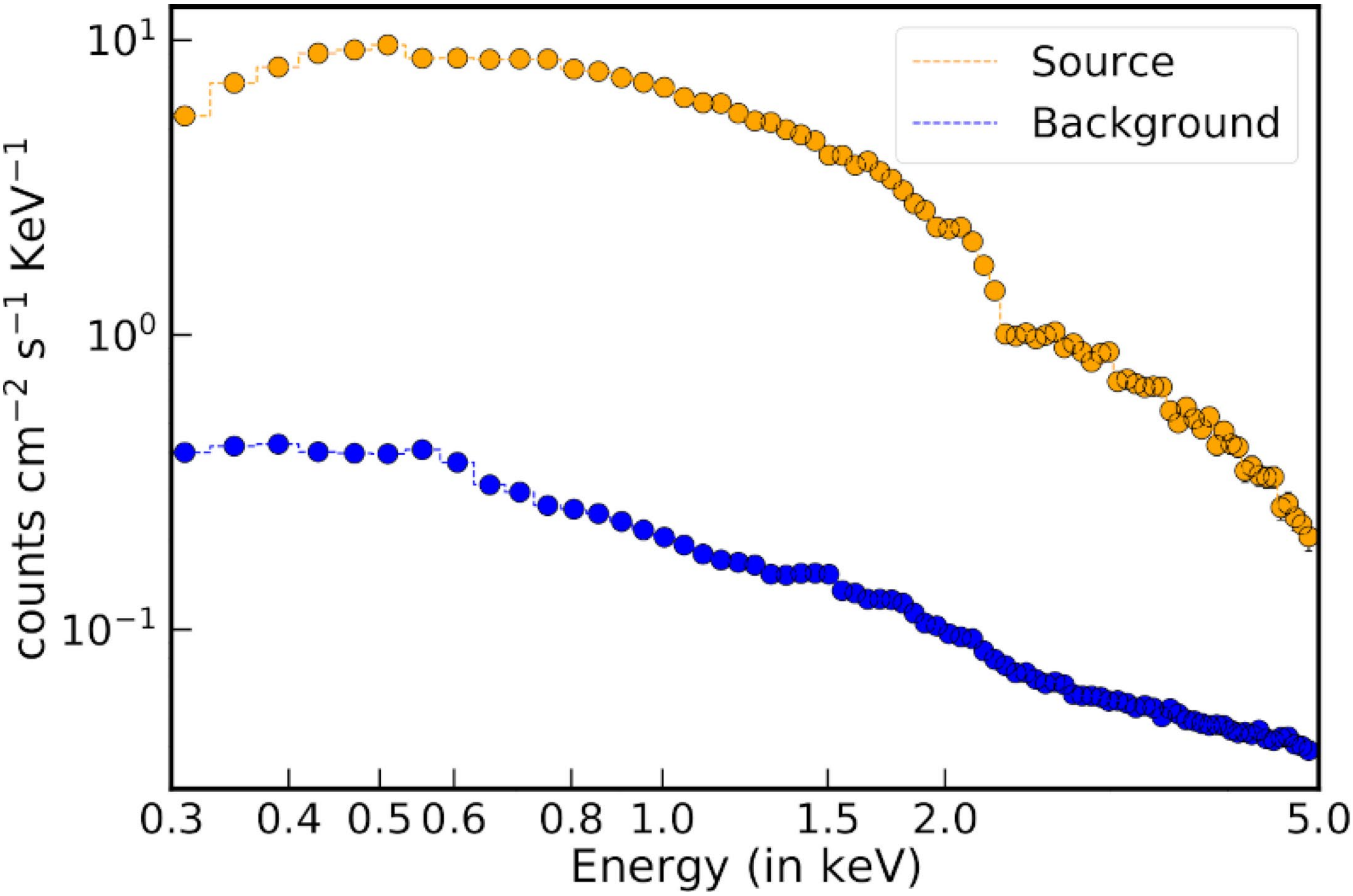

Extended Data Fig. 2 | A sample NICER X-ray spectrum. The orange and the blue data represent the source and the estimated background spectra, respectively. This particular dataset is from the E0 epoch of Table 1. The 1σ uncertainties are smaller than the data points.

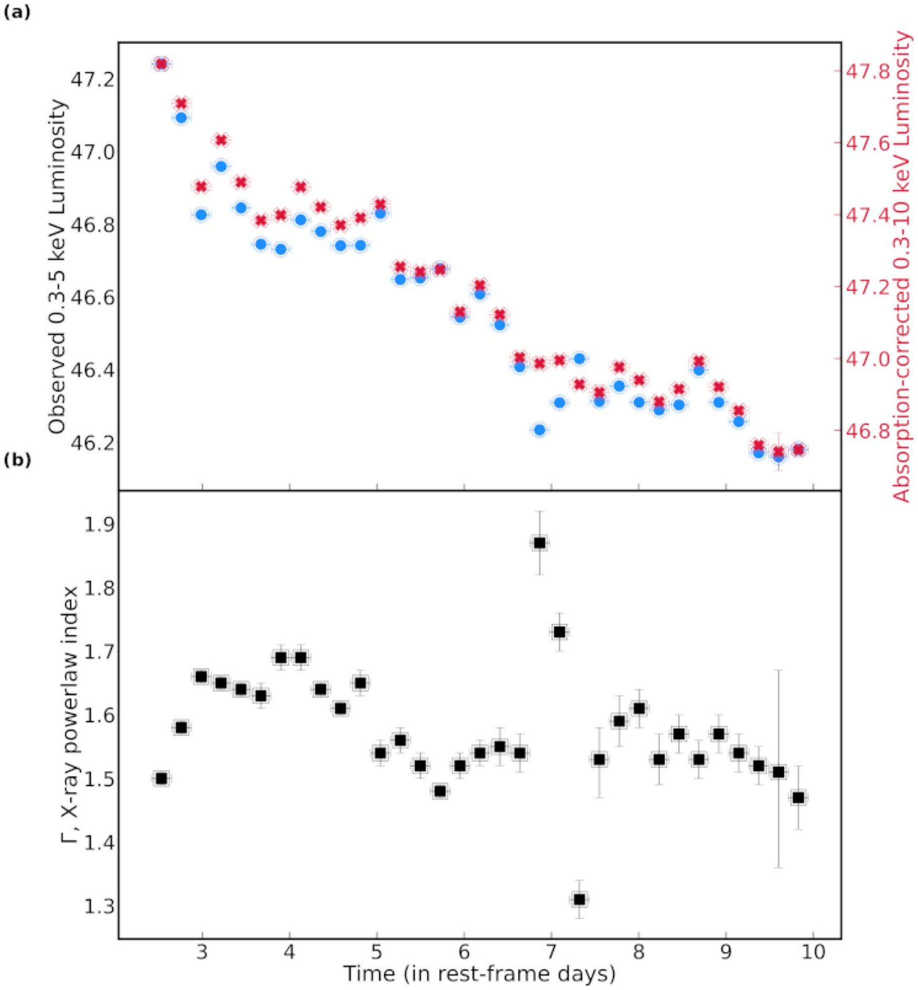

Extended Data Fig. 3 | AT 2022cmc's X-ray luminosity and energy spectral slope evolution. (a) Logarithm of the observed 0.3-5 keV (filled blue circles; left y-axis) and the absorption- corrected 0.3-10 keV luminosities (filled red crosses; right y-axis) in units of ergs s^{1}. The error bars on the luminosities are much smaller than the size of the data points. (b) Evolution of the best-fit power-law index with time. The abrupt changes in index around day 7 (rest-frame) coincide with a hard X-ray (2-5 keV) flare that happened during epoch E21 (the data point with best-fit photon index of ~ 1.3; see Table 1). The neutral Hydrogen column of the host was tied across all epochs and the best-fit value is (9.7 ± 0.3) × 10^{21} cm^{2}. All the error bars represent 1σ uncertainties. The individual NICER spectra are provided as supplementary data.

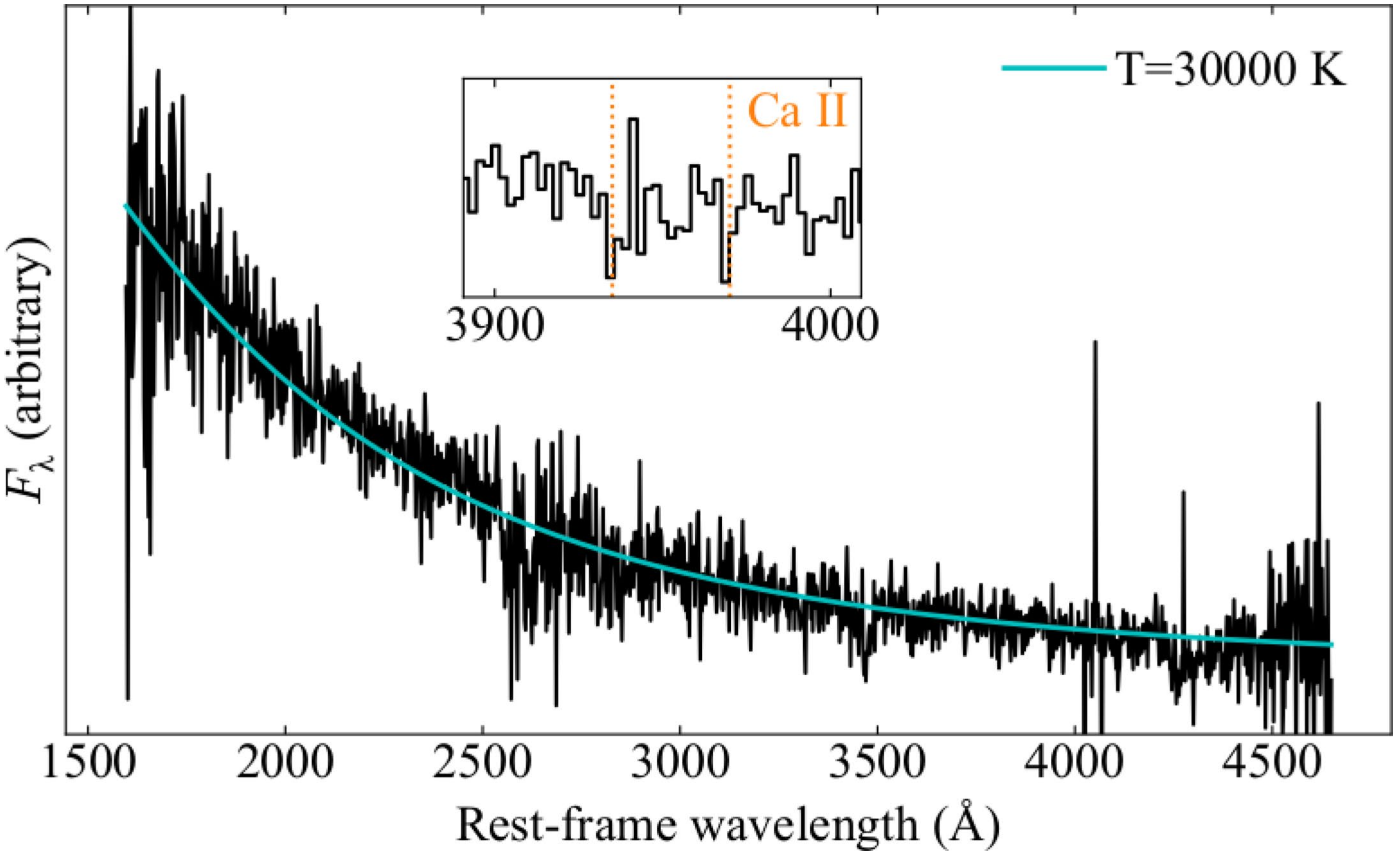

Extended Data Fig. 4 | VLT/X-shooter spectrum of AT2022cmc, obtained at ≈ 15 days after discovery. The featureless blue continuum can be modelled with a blackbody with T ≈ 30,000 K (solid blue line), consistent with the optical bump in the broad-band SED from day 25-27 (Fig. 3). The inset shows a zoom in on the region with CaII absorption lines identified by (7).

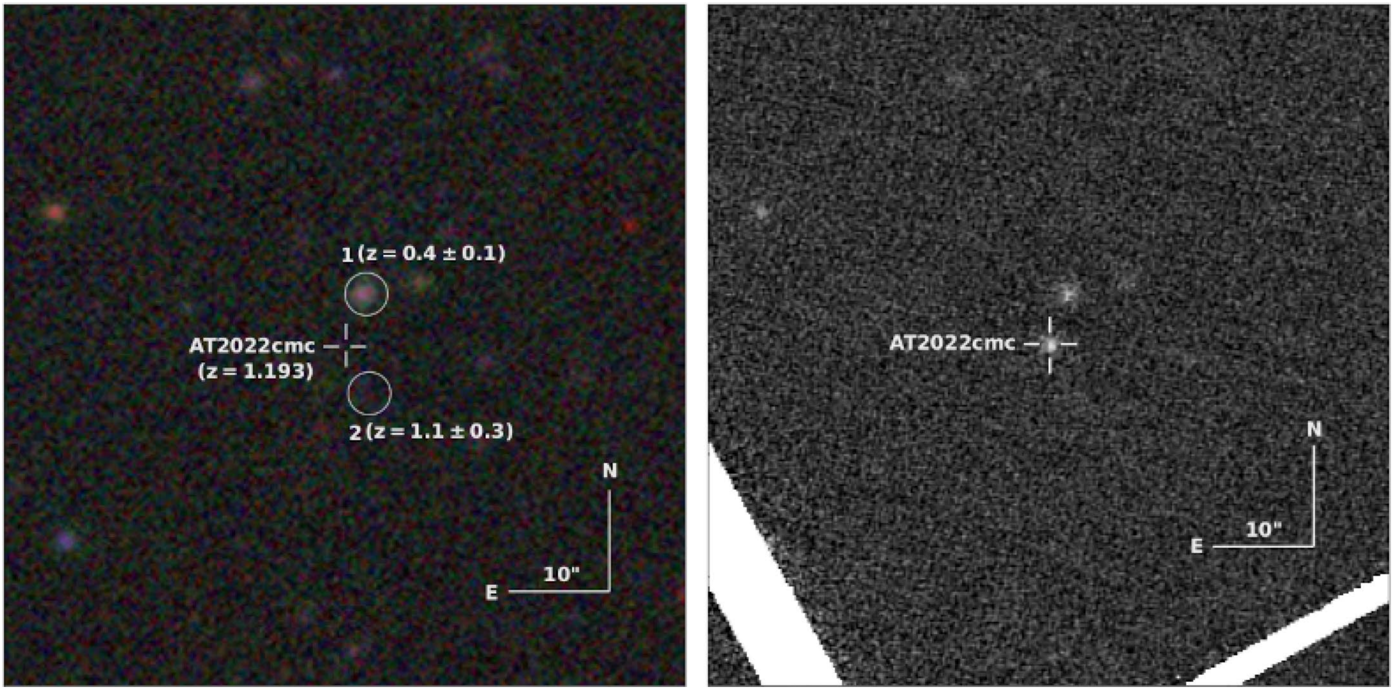

Extended Data Fig. 5 | Pre and post-outburst optical images of AT2022cmc. Left panel: A colour composite image of the field prior to the outburst, made using data from the Legacy Imaging Surveys (140) using g, r and z filters. There is no emission at the location of AT2022cmc (cross). Nearby catalogued objects with their photometric redshifts are shown (circles). Right panel: A PS2 w-band image of AT2022cmc post outburst. The size of both image cutouts is 1.1′ × 1.1′. North and the East arrows are each 10″.

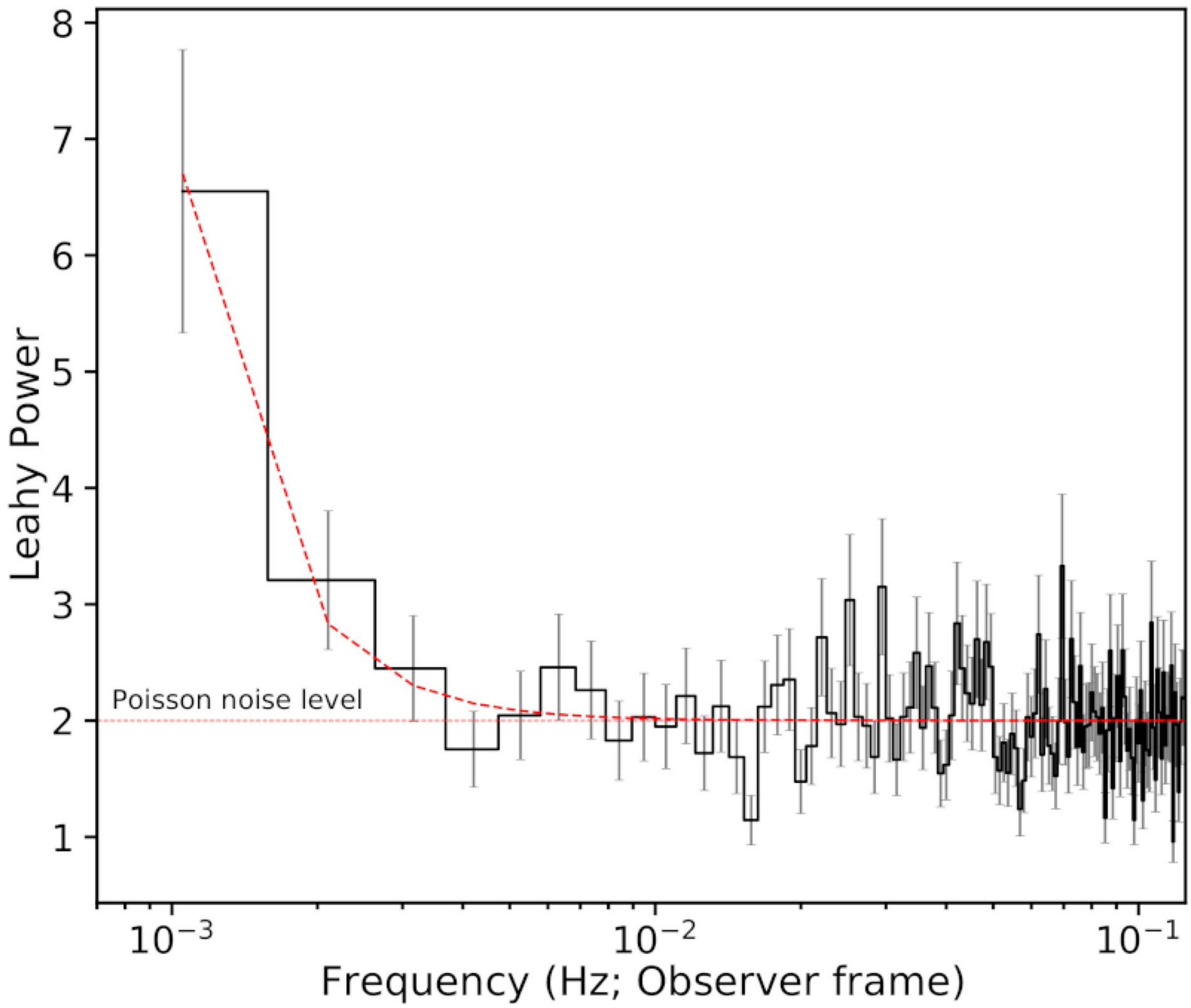

Extended Data Fig. 6 | Average X-ray (0.3-5 keV) power density spectrum of AT2022cmc. The frequency resolution and the Nyquist frequency are 1/950 Hz and 1/8 Hz, respectively. This power spectrum is an average of 29 individual PDS. The dashed, red curve is the best-fit power-law model. Systematic variability on timescales of ~ 1000 s (lowest frequency bin) is evident. All the frequencies and hence the timescales are as measured in the observer frame. The error bars represent 1σ uncertainties.

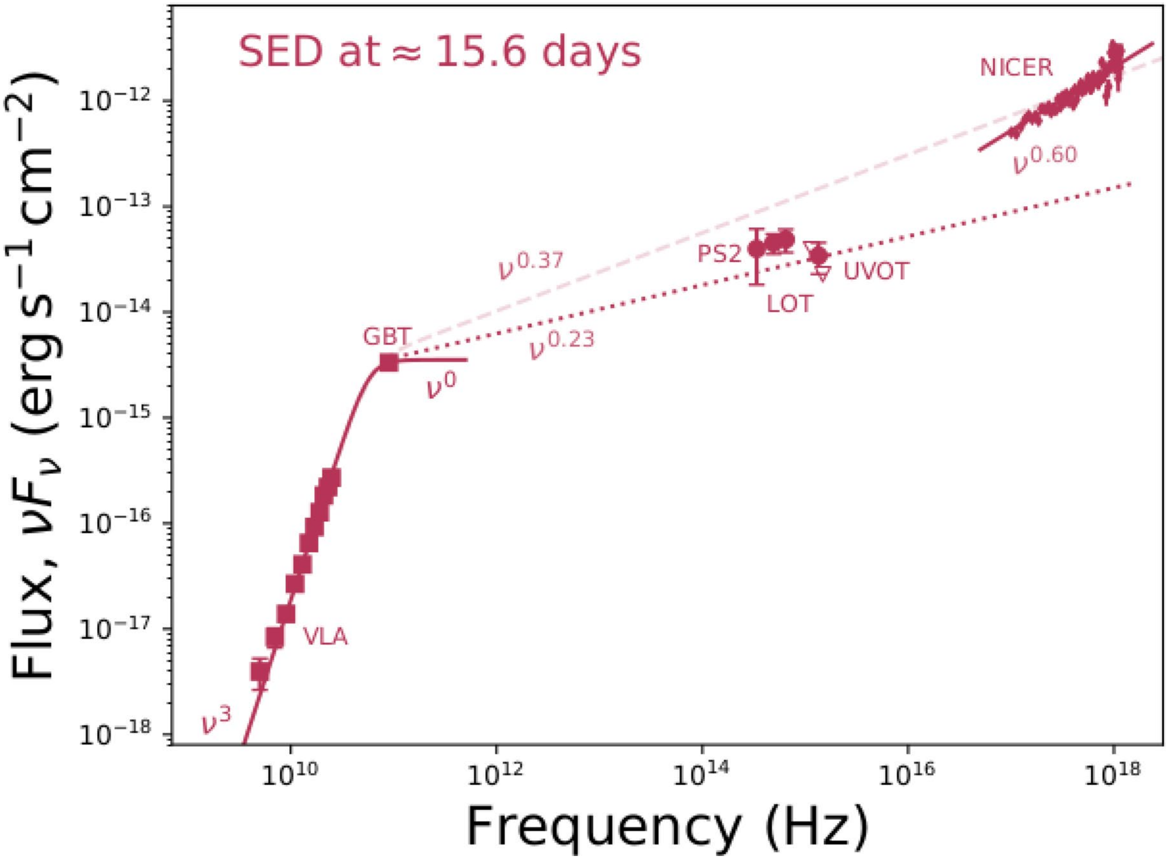

Extended Data Fig. 7 | Spectral energy distribution of AT2022cmc at ≈ 15.6 days after discovery. Data at radio (VLA), mm-band (GBT), UV/optical (*Swift*/UVOT, ZTF, PanSTARRS) and X-ray frequencies (NICER), demonstrate that the SED at this time cannot be explained as a single synchrotron spectrum. The SED at ≲ 25 GHz is optically thick ($\nu F_\nu \propto \nu 3$), with a spectral break near ≈ 90 GHz. The spectral index from the GBT observation at ≈ 90 GHz to the NICER band is $\nu F_\nu \propto \nu^{0.37}$, which (i) is substantially shallower than the observed NICER spectral index ($\nu F_\nu \propto \nu^{0.57}$) and (ii) over-predicts the UV flux at this time. All the error bars represent 1σ uncertainties.

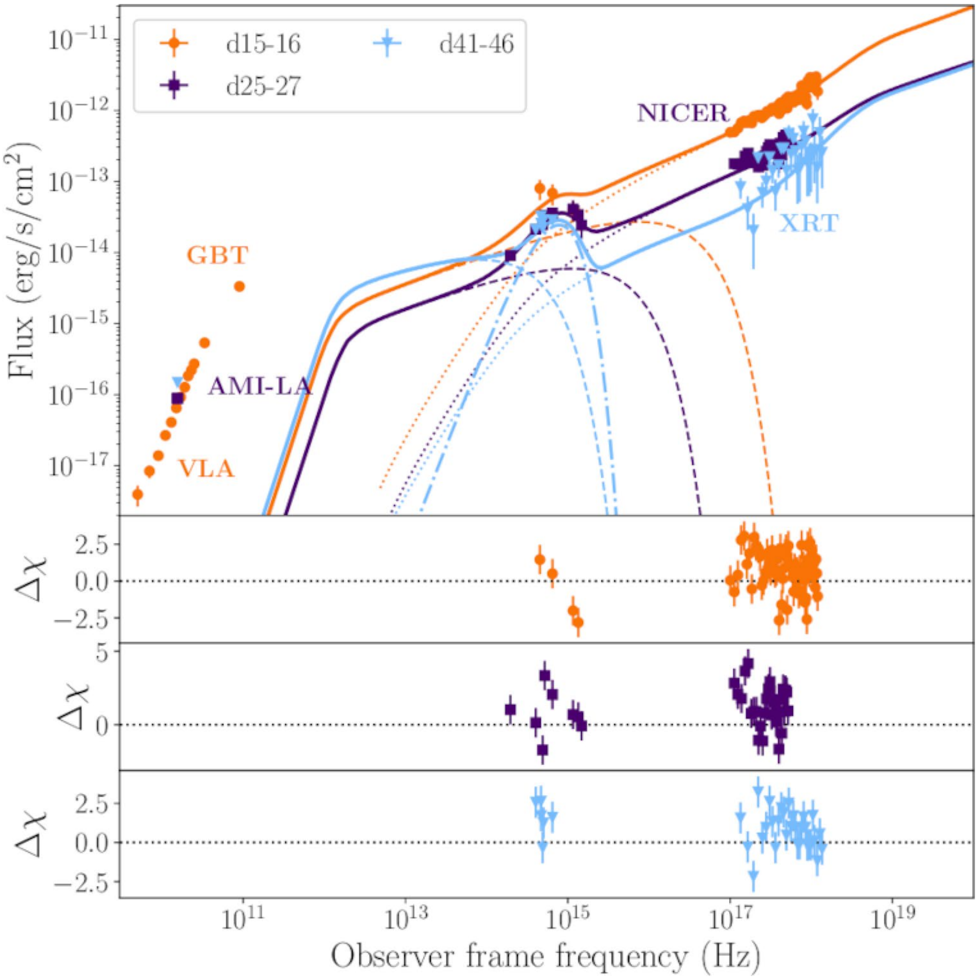

Extended Data Fig. 8 | Best fitting External inverse Compton (EC) model. The EC model requires a jet that under-predicts the radio flux. Furthermore, EC produces too little soft X-ray flux, and as in model 1 the emission at these frequencies is dominated by SSC. All the error bars represent 1σ uncertainties.

https://doi.org/10.1038/s41550-022-01820-x

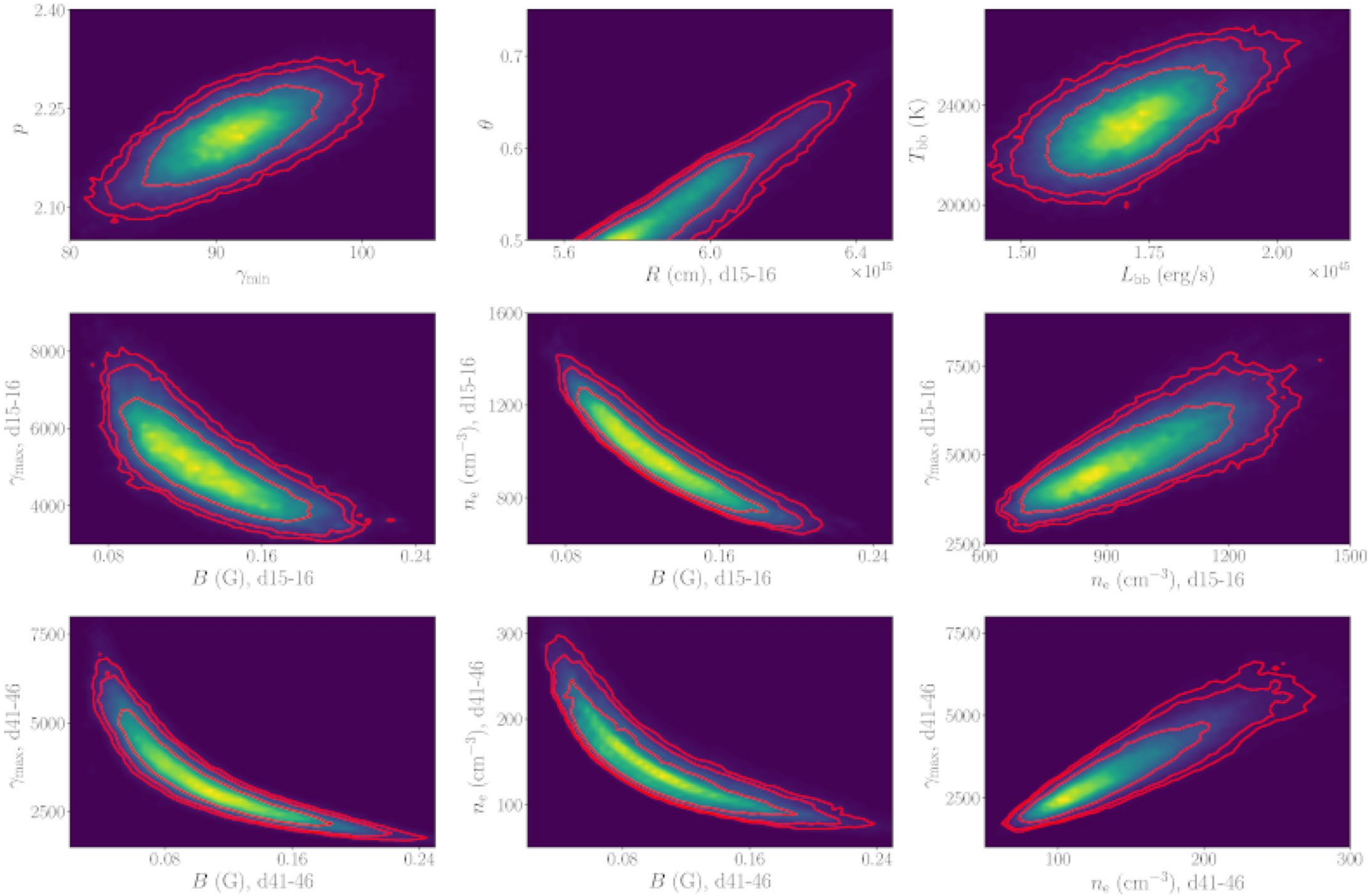

Extended Data Fig. 9 | Contour plots for the best-fitting parameters of model 1. For clarity, we only show the 2d posterior distributions of parameters that are degenerate with each other.